Algorithm Theoretical Baseline Document - MVIRI FCDR Release 1

DOI data 0-degree mission:	***10.15770/EUM_SEC_CLM_0009***
DOI data IODC 57-degree mission:	***10.15770/EUM_SEC_CLM_0012***
DOI data IODC 63-degree mission:	***10.15770/EUM_SEC_CLM_0013***

Doc.No. : EUM/OPS/DOC/18/990143
Issue : v3A e-signed
Date : 31 August 2020
WBS/DBS :

EUMETSAT
Eumetsat-Allee 1, D-64295 Darmstadt, Germany
Tel: +49 6151 807-7
Fax: +49 6151 807 555
http://www.eumetsat.int

Document Change Record

Version	***Version Date*** *(as on profile)*	***DCR* No.*** *if applicable*	***Description of Changes***
v1E	1 January 2019		Final version ready for internal review
v2A	06 March 2020		Initial version ready for DRR
v3	3 August 2020		Final version
V3A	31 August 2020		Some type setting issues were identified during the approval loop, which is rectified in this version.

****DCR = Document Change Request***

Table of Contents

1 INTRODUCTION

1.1 Purpose of this Document

This Algorithm Theoretical Baseline Document (ATBD) provides detailed information on the physical principles of the methodologies that have been used to generate the first release of the Fundamental Climate Data Record (FCDR) of recalibrated Level 1.5 Infrared (IR), Water Vapour (WV), and Visible (VIS) radiances from the Meteosat Visible Infra-Red Imager (MVIRI) instruments (MVIRI FCDR Release 1) onboard Meteosat First Generation (MFG) satellites. The released data record covers about 35 years of data (4 February 1982 till 4 April 2017) and can be regarded as a true Fundamental Climate Data Record, i.e., it is a long-term data record of calibrated and quality-controlled sensor data, designed to allow the generation of homogeneous products that are accurate and stable enough for climate monitoring and data assimilation in reanalysis of the recent climate. This ATBD aims to:

1. Give background information on the activities that initiated the implementation of the algorithms presented in this ATBD;
2. Provide a description and discussion of physical principles of the algorithms for the recalibration of visible, infrared and water vapour observations implemented in the reprocessing chain, including scientific background, a justification of the used algorithms, as well as information on the parameterisation used;
3. List constraints and limitations of the presented algorithms.

1.2 Structure of this Document

1.3 Acronyms

The following table lists definitions for all acronyms used in this document.

Acronym	Meaning
ADC	Atlantic Data Coverage
AIRS	Atmospheric Infrared Sounder
AMV	Atmospheric Motion Vector
ATBD	Algorithm Theoretical Baseline Document
CDR	Climate Data Record
CM SAF	Satellite Application Facility on Climate Monitoring
ECMWF	European Centre for Medium-Range Weather Forecasts
ERA-CLIM	European Re-Analysis of global Climate observations

EUMETSAT	European Organisation for the Exploitation of Meteorological Satellites
FCDR	Fundamental Climate Data Record
FOV	Instantaneous Field of View
GCOS	Global Climate Observing System
HIRS	High Resolution Infrared Sounder
IASI	Infrared Atmospheric Sounding Interferometer
IMAG2TG	Non-Rectified Image File (as produced by the MFG Image Processing System)
IODC	Indian Ocean Data Coverage
IR	Infrared
MARF2TG	Meteorological Archive & Retrieval Facility self-describing format
MFG	Meteosat First Generation
MSG	Meteosat Second Generation
MSICC	Multi Sensor Infrared Channels Calibration
MVIRI	Meteosat Visible Infra-Red Imager
NASA	National Aeronautics and Space Administration
netCDF	Network Common Data Form
NOAA	National Oceanographic and Aeronautical Administration
PICS	Pseudo Invariant Calibration Sites
RECT2LP	Rectified Image File (as produced by the MFG Image Processing System)
RMSD	Root Mean Square Difference
SEVIRI	Spinning Enhanced Visible and Infra-Red Imager (on MSG satellites)
SI	International System of Units
SNO	Simultaneous Nadir Overpass
SRF	Spectral Response Function
SSCC	SEVIRI Solar Channel Calibration
SSP	Sub-Satellite Point
STAMP	Space Time Angle Matchup Program
UMARF	Unified Meteorological Archive & Retrieval Facility
VAX	Virtual Address eXtension
VIS	Visible
WMO	World Meteorological Organisation
WV	Water Vapour
XADC	Extended Atlantic Data Coverage

1.4 Symbols

The following table lists the symbols used in this document.

Symbol	Meaning
$\tilde{L}$	Band integrated radiance
L	Spectral radiance
ϕ	Spectral response function
λ	Wavelength
c_5	Five-day count-radiance ratio value
$u_i(c_5)$	Independent uncertainty of a five day count-radiance ratio
$u_s(c_5)$	Structured (correlated) uncertainty of a five day count-radiance ratio
$S_\phi(\lambda,\lambda')$	covariance of the spectral response function as function of wavelengths
$u_\phi(\tilde{L})$	uncertainty of the band integrated radiance due to uncertainties in the spectral response function
a_{cf}	Calibration coefficient interpolated from a polynomial fit across all c_5 values of a satellite
a_0, a_1, a_2	Parameters of the polynomial fit across all c_5 values of a satellite
C	Effect Sensitivity Matrix
U	Effect Uncertainty Matrix
R	Effect Correlation Matrix
$u(+0)$	Uncertainty attributed to the fiduceo +0 term
θ	Solar zenith angle
δ	Solar declination
ω	Local hour angle
$\tilde{R}$	Band integrated top-of-atmosphere bidirectional reflectance
$\tilde{E}_{0,sun}$	Band integrated solar Irradiance
d	Sun-earth distance in astronomical units
$\bar{C}_E$	Rectified (=interpolated) earth count
$\bar{C}_S$	Mean space corner count value (=dark signal)
σ_τ	Allan deviation
$u_X(Y)$	Example notation: Uncertainty in Y caused by X
c	A single sensitivity coefficient

1.5 Definitions

The following definitions are used throughout the document.

Data levels:

- Level-1.0 - Instrument data at full original resolution as measured counts with geolocation and calibration information attached but not applied [RD 4]. These are not available in the FCDR, but are archived.
- Level 1.5 – Instrument counts (as available in Level-1.0) mapped (rectified) onto a geostationary projection grid for each orbital position, as if the satellite were truly in a fixed location and a fixed scanning geometry. Instrument pixels have been averaged over 4 by 4 Level-1.0 pixels (cubic-spline). These are available in the FCDR.

Harmonisation and Homogenisation:

- Harmonisation of a dataset is equivalent to a consistent recalibration of a series of instruments. The observations represent the physics of each instrument, in particular the spectral weighting of the incoming light by the spectral response functions. As the spectral response functions differ for instruments, jumps due to instrument switches are expected.
- Homogenisation of a dataset uses a-priory knowledge about the spectrum of the observed target to adjust the differences between spectral response functions. For the visible band homogenisation is particularly challenging: The band adjustment functions between two instruments remain constant for different brightness levels, but they lose validity as soon as the shape of the target spectrum changes. This can happen e.g. due to cloud contamination or natural seasonality. Jumps due to instrument switches are not expected.

Product types:

- Fundamental Climate Data Record [RD 3] - is a well-characterised, long-term data record, usually involving a series of instruments, with potentially changing measurement approaches, but with overlaps and calibrations sufficient to allow the generation of products that are accurate and stable, in both space and time, to support climate applications. FCDRs are typically calibrated radiances, backscatter of active instruments, or radio occultation bending angles. FCDRs also include the ancillary data used to calibrate them.

Uncertainty terminology (see details in RD 6 and RD 7):

- Independent - "Independent errors arise from random effects causing errors that manifest independence between pixels, such that the error in L(l′,e′) is in no way predictable from knowledge of the error in L(l,e), were that knowledge available. Independent errors therefore arise from random effects operating on a pixel level, the classic example being detector noise." [RD 7]
- Structured - "Structured errors arise from effects that influence more than one measured value in the satellite image, but are not in common across the whole image. The originating effect may be random or systematic (and acting on a subset of pixels), but in either case the resulting errors are not independent, and may even be perfectly correlated across the affected pixels. Since the sensitivity of different pixels/channels to the originating effect may differ, even if there is perfect error correlation, the error (and associated uncertainty)

in the measured radiance can differ in magnitude. Structured errors are therefore complex, and, at the same time, important to understand, because their error correlation properties affect how uncertainty propagates to higher-level data." [RD 7]

- Common - "Common errors are constant (or nearly so) across the satellite image, and may be shared across the measured radiances for a significant proportion of a satellite mission. Common errors might typically be referred to as biases in the measured radiances. Effects such as the progressive degradation of a sensor operating in space mean that such biases may slowly change." [RD 7]
- Uncertainty and Error - "Some metrologists avoid the word 'error' to avoid the confusion arising from incorrect usage of 'error' and 'uncertainty' in much scientific literature. There is often no ambiguity in the case of a repeated measurement in a laboratory, where the dispersion in measured values arises solely from the dispersion of measurement errors. But, in EO, it is essential to distinguish the dispersion in measured radiances due to geophysical variability (signals of interest) from the dispersion due to measurement errors. To maintain that distinction, we find it necessary to use terms such as 'error correlation' and 'error covariance' intentionally and consistently." [RD 7]

Other:

- Monitored sensor – refers to the sensor that is subject to (re)calibration.
- Reference sensor – refers to the sensor, preferably with superior quality, which is used as (re)calibration reference.

2 BACKGROUND INFORMATION

The generation of the MVIRI FCDR Release 1, for which the algorithms presented in this ATBD were used, was triggered by two European Commission funded projects, i.e., the EU FP7 European Re-Analysis of the global CLIMate system (ERA-CLIM) 2 project [RD 5] and the EU H2020 Fidelity and uncertainty in climate data records from Earth Observations (FIDUCEO) project [RD 6]. In the framework of ERA-CLIM2, the algorithms have been developed for the recalibration of infrared and water vapour observations from geostationary satellites. In the framework of FIDUCEO, the algorithms have been developed to recalibrate the visible channel observations from geostationary satellites. These algorithms have been applied to MVIRI data collected onboard MFG satellites to generate the MVIRI FCDR Release 1 covering the years 1982 -2017.

The infrared and water vapour channel data from this FCDR are used for assimilation into European Centre for Medium-Range Weather Forecasts (ECMWF) global reanalyses, but these observations can also be used in regional reanalysis efforts. In the FIDUCEO project, the visible channel data from this FCDR are being used for the retrieval of an albedo and aerosol Climate Data Record (CDR). EUMETSAT's Satellite Application Facility on Climate Monitoring (CM SAF) [RD 8] is using the FCDR for generating time-series of cloud amount, land surface temperature and other climate variables from MFG observations. In the framework of the Copernicus Climate Change Service (C3S) project (see https://climate.copernicus.eu/) this FCDR will serve as input to the Atmospheric Motion Vectors (AMV) algorithm to derive a climate data record of upper air wind speed and direction.

3 SATELLITE SENSORS

This section gives an overview of the characteristics of the instruments used to generate the MVIRI FCDR Release 1 of visible (VIS), infrared (IR) and water vapour (WV) radiances.

3.1 Monitored instrument - MVIRI

3.1.1 Sensor characteristics

The MVIRI instrument was operated on-board EUMETSAT's MFG series of European geostationary satellites during the years 1977 – 2017. The MFG series consisted of 7 satellites. The first MFG satellite (Meteosat-1) was launched in 1977 but failed in late 1979. Meteosat-2 took up operations in late 1981 and since then an unbroken data record exists. However, The Meteosat-1 data were not used for the data record provided in MVIRI FCDR Release 1.

The MFG satellites were spin-stabilized and positioned at an altitude of about 36000 km above the equator. The nominal sub-satellite longitude for the zero-degree mission was at 0°, for the Atlantic Data Coverage (ADC) mission at 50° W, for the eXtended Atlantic Data Coverage (XADC) mission at 75° W, and for the Indian Ocean Data Coverage (IODC) missions at 57° (Meteosat-7), 63° (Meteosat-5), and 67° E (Meteosat-6). Data from the ADC and XADC missions were not considered for the FCDR. From the IODC mission, only the 57° (Meteosat-7) and the 63° (Meteosat-5) missions are included.

The MVIRI instrument scanned the complete disk of the Earth two times per hour, and operated 3-channels simultaneously. There was one broadband solar channel, one infrared window channel, and one water vapour absorption channel. The infrared window channel measured radiation emitted by Earth's surface in clear-sky conditions or from a cloud top. The water vapour channel measured radiation emitted by water vapour in the upper troposphere (a broad layer roughly between 500 and 200 hPa, and slightly variable depending on the humidity content of the atmosphere). The nadir spatial sampling of MVIRI was 2.25×2.25 km for the visible channel, and 4.5×4.5 km for the infrared and the water vapour channels.

Table 1 summarizes the spatial sampling and the spectral characteristics for the visible, infrared, and water vapour channels of MVIRI. A detailed list of the operational periods for each MFG platform can be found in [RD 25].

Table 1: *Spatial and instrumental characteristics of MVIRI visible (VIS), thermal infrared (IR), water vapour (WV) channels.*

Channel	*Detectors*	*Digitisation*	*Sampling at nadir (km)*	*Pixel grid size*	*Nominal central wavelength (μm)*
VIS	2	6 bit/8bit	2.25	5000x5000	0.7
WV	1	8bit	4.5	2500x2500	6.4
IR	1	8bit	4.5	2500x2500	11.5

Figure 1 presents the standard pre-launch spectral response functions of MVIRI's broad solar or visible channel that is sensitive to reflected light with wavelengths between 0.3 and 1.2 μm. It has been shown that this channel was affected by inaccurate pre-flight characterisations [RD 19, RD 20] and spectral degradation during the lifetime of each satellite [RD 21]. This ATBD describes the approach adopted to derive reconstructed spectral response functions and their degradation using inverse techniques [RD 9, RD 10].

Figure 2 presents the band positions of MVIRI's WV and IR channels that are sensitive to thermal radiation emitted with wavelength between 5.70 - 7.10 μm and 10.50 - 12.50 μm, respectively. This figure shows that the Spectral Response Functions (SRFs) of the WV channel Meteosat-2 and -3 differ significantly from those of Meteosat-4, -5, -6, and -7.

Note that for Meteosat-2 and -3, the data from the IR channel and of the first VIS channel detectors was received on a 30-minute basis. To fit within bandwidth constraints, the data of the WV and the second VIS channel detector were downlinked alternately. In effect, the temporal resolution for these channels is therefore only hourly. Moreover, the data of WV and VIS channels on these two satellites were digitised into 6-bit data (and 8-bit for the IR channel) rather than into 8-bits as on the later satellites, leading to a poorer image quality.

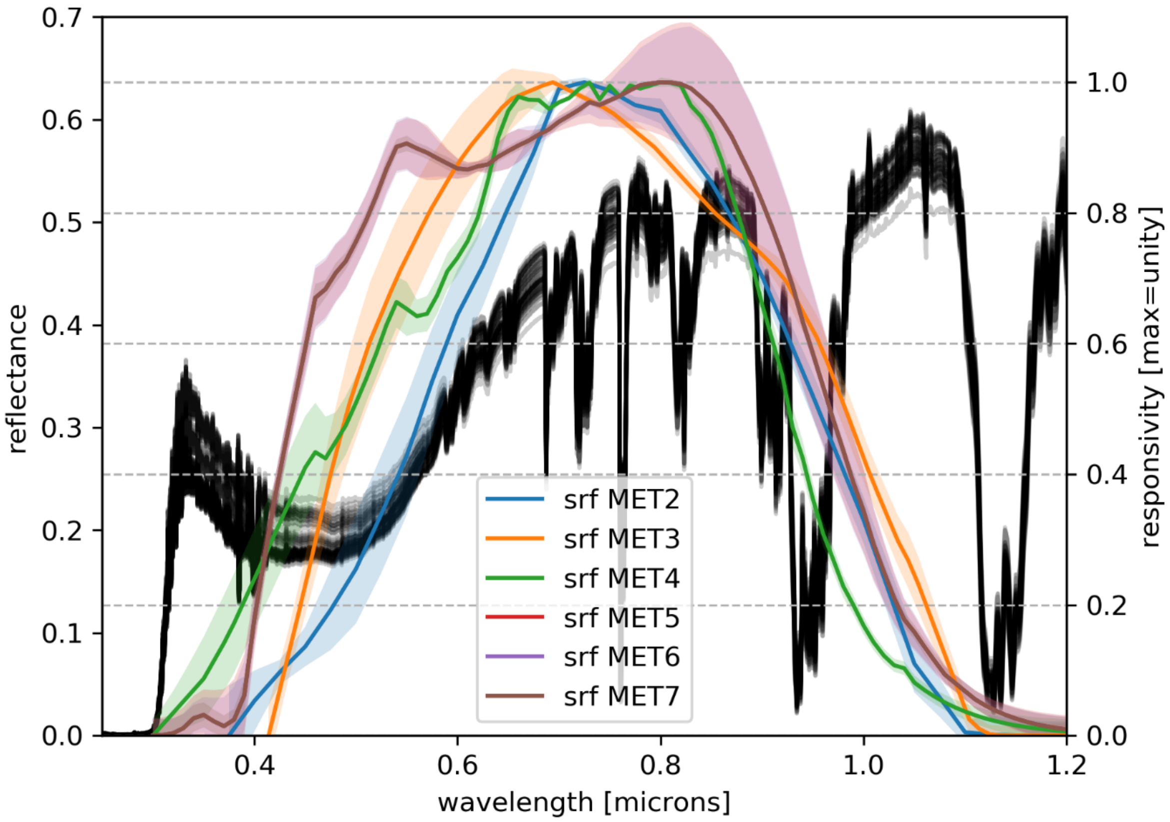

Figure 1: *Normalised, original SRFs of MVIRI VIS channel on-board Meteosat-2 to Meteosat-7. Example SCIAMACHY reflectance spectra collected during 2002 over Algeria are shown in black. The SRFs for MET5, 6 and 7 are overlaid because they were considered the same, but only the uncertainties differ slightly.*

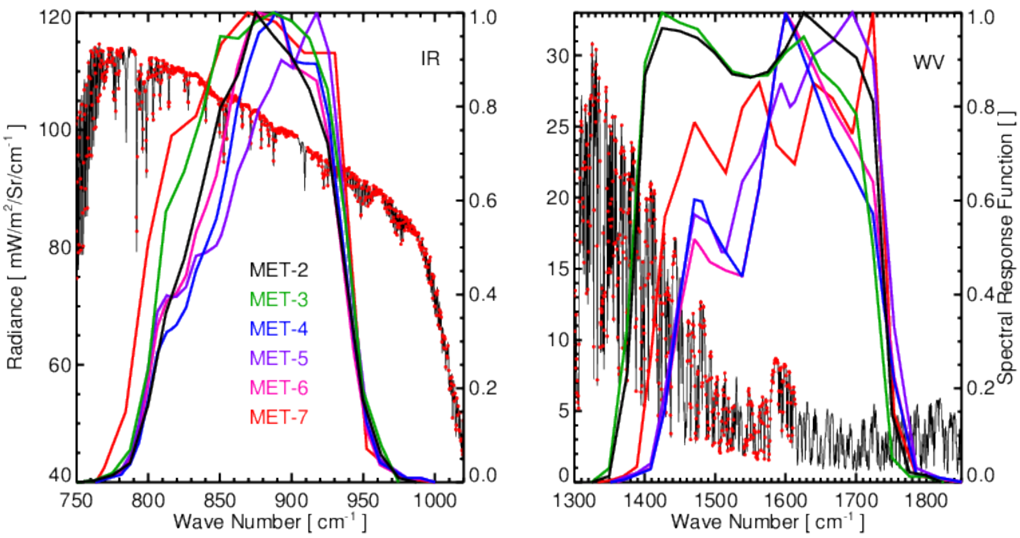

Figure 2: *Normalised SRF of MVIRI IR (left) and WV (right) channels on-board Meteosat-2 to Meteosat-7. An example IASI spectrum is shown in black and a IASI spectrum interpolated to the AIRS frequency grid is shown in red dots to provide an indication of gaps in the AIRS spectrum inside MVIRI bands.*

3.1.2 Data used for the FCDR

The main source of information for generating the FCDR are geo-rectified MVIRI images (Level 1.5) that are stored in the binary RECT2LP format. In these files, the Virtual Address eXtension (VAX) representation of floats is used for most variables. The metadata are contained in three headers and one trailer record. For each image the line record also holds short header/trailer information, referred to as “line headers/trailers”. The RECT2LP format only contains the forward scan, whereas the backwards scan and the space counts are masked out. A detailed format description is given in RD 12.

Information on additional image headers, on telemetry data and on the counts of the space corners is obtained from the non-rectified Level 1.0 MVIRI data. MVIRI raw images (Level 1.0) are stored in the binary Meteorological Archive & Retrieval Facility self-describing (MARF2TG) format. This format was developed for storage reasons only. Any processing of the data usually relies on the, better documented, IMAG2TG format (RD 13 pages 101 ff.). This format is organised in 3069 records of 17296 bytes. Records 1-39 are headers, records 40-3069 hold the image lines from forward and backward scan. Telemetry records for ~5 minute intervals are split over the first bytes of multiple-line records. IMAG2TG files are exploited for the FCDR to retrieve some additional header fields (e.g. orbit coordinates in mean geocentric format) and telemetry data for the FCDR. Also the counts of space corners are stripped from the images in order to evaluate the dark signal and the electronics noise.

4 VISIBLE RECALIBRATION AND UNCERTAINTY ANALYSIS

4.1 Overview

This section presents the theoretical basis of the methodologies used for the consolidation and uncertainty analysis of the visible channel measurements of MVIRI onboard MFG satellites. The methodology is published in a peer-reviewed paper [RD 31] and captured in Figure 3 that provides a flow diagram of it. The recalibration makes use of reconstructed SRFs (section 4.2.1). These SRFs are ingested into a version of the MSG SEVIRI Solar Channel Calibration (SSCC) algorithm [RD 11, RD 16] adapted for MVIRI. The algorithm adopts a vicarious calibration approach for recalibrating VIS channel measurements of MVIRI (section 4.2.2). The calibration coefficients, the reconstructed SRFs and the calculation of the illumination geometry (section 4.2.3) are included in the uncertainty analysis of the measurements (section 4.3). The analysis is performed for each individual effect in the measurements giving rise to uncertainty. Those data are provided to specialist users as the so-called fullFCDR dataset. For the broader user community the uncertainties arising from all effects are combined into a structured and independent uncertainty on a pixel-basis. Those data are provided as the so-called easyFCDR [RD 2].

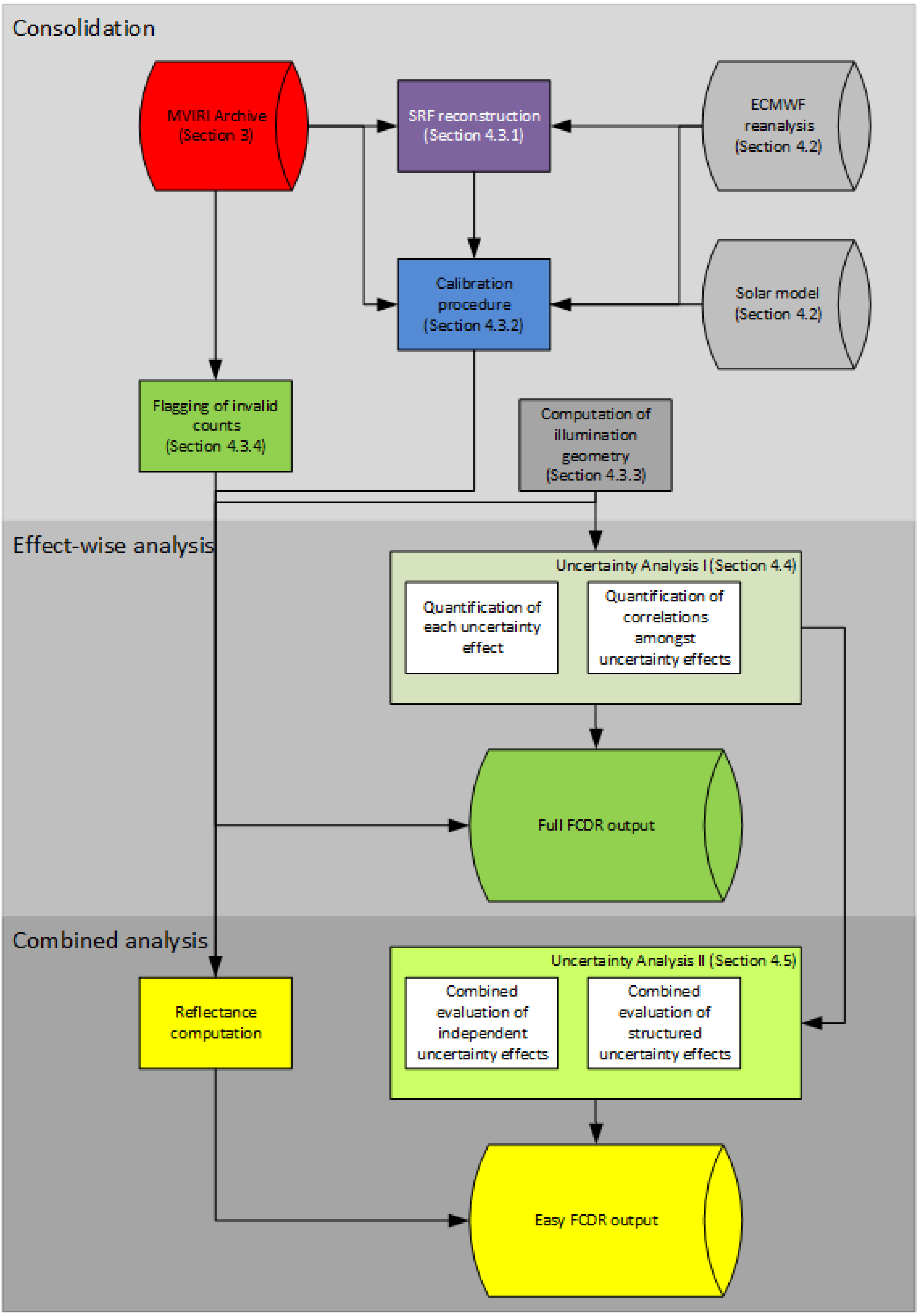

Figure 3: *Overview of the generation process for the MVIRI VIS FCDR.*

4.2 Input

Besides the satellite sensor input (see section 2), the visible calibration algorithm requires ECMWF atmosphere data and a solar spectrum model as input.

ECMWF atmosphere data

The radiative transfer simulation of the calibration and of the SRF reconstruction require atmospheric parameters that are extracted from ERA Interim forecasts [RD 35]. The fields that are used in our retrieval are surface pressure, total column water vapour and 10 m U- and V-winds.

Solar spectrum model

The solar spectrum model used for the FCDR generation is described in [RD 14]. It is consistent with the solar spectrum model used for the calibration and for the reconstruction of the SRF.

4.2.1 SRF reconstruction – Algorithm Summary

Metrologically-sound techniques used for the reconstruction of the VIS spectral response functions is described in detail in [RD 9] and [RD 10]. The methodology relies on: i) simulated radiance spectra [RD 10] at Pseudo-Invariant Calibration Sites (PICS). The PICS considered here are the Libya-4 desert site [RD 34], several ocean targets, and Deep Convective Clouds (DCCs) over land and ocean and ii) extracted MVIRI digital counts for these PICS. The simulations are performed using a state-of-the-art radiative transfer model (LibRadTran version 2) for appropriate viewing geometries and atmospheric conditions of the extracted digital counts. Ancillary atmospheric information are gathered from reanalyses and other satellite based datasets. Meaningful prior response functions are defined and represented using Bernstein polynomials. These SRFs together with other MVIRI instrument specifications, e.g., gain setting, and the simulated spectra are used to obtain simulated counts. The residuals between observed and simulated counts are considered as a measure of the precision of the response function. An inverse algorithm [RD 9] is then applied to optimise the residuals by tuning the shape of the Bernstein polynomials and of the parameterisation of the instrument aging model.

4.2.2 Calibration – Algorithm Summary

The recalibration of the MVIRI VIS imagery builds upon the operational MSG SEVIRI Solar Channel Calibration System (SSCC) [RD 11]. The SSCC system conducts radiative transfer modelling above pseudo invariant calibration sites (desert and sea). The simulated radiances are then related to the corresponding satellite measurements. Outliers, such as observations with cloud- or aerosol-contamination, are rigorously removed [RD 10]. The radiative transfer model in use is 6S [RD 15]. Count-radiance ratios c are collected over five-day periods and then combined (mean value weighted by individual uncertainty) into one value, which will be denoted by c_5. Ratios of subsequent five-day runs are analysed using orthogonal distance regression methods for throughout the lifetime of each satellite to derive the recalibration parameters. Uncertainty propagation through this process is complex and has to consider potential error correlations between the results of the subsequent five-day runs. Therefore, the uncertainty of the five-day count-radiance ratios is separated into four different components: The intrinsic radiative transfer model uncertainty, the uncertainties of the surface and atmosphere characterisation, the noise of the satellite counts and the uncertainty of the spectral response function (Table 2).

Table 2: *Uncertainty components of the count-radiance ratios that result from a five-day calibration run and the correlations between the errors of count-radiance ratios from multiple five-day calibration runs.*

Component	Error correlation	Justification
Intrinsic radiative transfer model uncertainty	Not correlated	Depends on illumination geometry which is different for each 5-day run due to different sets of discarded observations (e.g. due to cloudiness).
Surface characterisation uncertainty	Not correlated	The calibration includes up to 18 desert targets each having its own surface characterisation. The number and weighting the targets varies from 5-day run to 5-day run (e.g. due to cloudiness).
Atmosphere characterisation uncertainty	Not correlated	A systematic bias of the atmosphere parameterisation across the 18 different target sites and multiple days is assumed unlikely.
SRF uncertainty	Entirely correlated in time and between wavelengths	The SRF characterisation algorithm is executed once per satellite and therefore entirely correlated among all 5-day runs for a satellite.

The uncertainty of each count-radiance ratios value (c_5) is separated into 4 different components (see Table 3): *i)* the intrinsic radiative transfer model uncertainty ($u_m(c_5)$), *ii)* the atmosphere and surface parameterisation uncertainty ($u_p(c5)$), *iii)* the noise of the satellite counts ($u_r(c_5)$) and *iv)* the uncertainty of the spectral response function ($u_\phi(c_5)$). The SSCC system as presented in [RD 11] does not allow for the propagation of non-diagonal error covariance matrices. Firstly, it had to be updated to allow for the ingestion of the time-variant reconstructed spectral response functions (see [RD 9] and [RD 10]). To account for the wavelength-dependent error covariance that is provided with the recovered SRFs [RD 10] the method to propagate the spectral response function uncertainty was adopted according to [RD 22] and as described in [RD 16]. The simulated, band integrated radiance ($\tilde{L}$) is computed as follows:

$$\tilde{L} = \int_\lambda L(\lambda)\phi(\lambda)d\lambda \tag{1.1}$$

where $L(\lambda)$ denotes the spectral radiance, λ the wavelength, and ϕ the responsivity of the SRF. The uncertainty component of $\tilde{L}$ that results from the uncertainties of the reconstructed SRF ($u_\phi(\tilde{L})$) is given by:

$$u_\phi(\tilde{L}) = \int_\lambda \int_{\lambda'} L(\lambda)S_\phi(\lambda,\lambda')L(\lambda')d\lambda d\lambda' \tag{1.2}$$

where S_ϕ is the error covariance matrix of the SRF. In the subsequent processing steps the uncertainty of simulated radiances resulting from the SRF is then propagated as the $u_\phi(c_5)$ component of the uncertainty of each 5-day count-radiance ratio as described in [RD 11]. This error that causes this uncertainty is fully correlated for all calibration runs of one satellite.

In contrast to the SRF uncertainty, the $u_m(c_5)$, $u_r(c_5)$ and $u_p(c_5)$ uncertainties are expected to vary randomly from five-day run to five-day run. These uncertainties can be propagated to calculate the combined independent uncertainty of c_5 ($u_i(c_5)$) as follows:

$$u_i(c_5) = \sqrt{u_m(c_5)^2 + u_r(c_5)^2 + u_p(c_5)^2} \tag{2}$$

From the c_5 values of multiple five-day periods the calibration coefficient at launch (a_0) and the grey degradation with time (a_1) are retrieved for each satellite. In the past, the degradation was assumed to be well represented by a linear fit. However, it has become apparent for long-serving satellites, such as Meteosat-5 and Meteosat-7, that the degradation rate slows down with time (Figure 4). The calibration coefficient a_{cf} valid at time cf can be computed with:

$$a_{cf} = a_0 + a_1 Y + a_2 Y^2 + 0 \tag{3}$$

where Y denotes the number of years since launch, a_0, a_1, a_2 denote polynomial coefficients, and the 0 accounts for remaining uncertainties of the calibration model. In order to take account for the slowing degradation a non-linearity term (a_2Y^2) is added to Eq. (3). The fitting of the calibration parameters a_0, a_1, a_2 is carried out by applying orthogonal distance regression on subsequent 5-day calibration results for the full time-series of each satellite. Weighting is done based on the inverse of the squared combined uncertainty ($u_i(c_5)$ and $u_\phi(c_5)$) of each run. The covariance of the parameters of the orthogonal distance regression fit is computed from the residuals of the polynomial model Eq. (3). However, this does not account for errors that are correlated between calibration runs, such as errors in the characterization of the SRF. As those errors would not appear in the residuals, they are propagated, using the $+0$ term, as follows:

$$u(+0) = C \cdot U \cdot R \cdot U^T \cdot C^T \tag{4}$$

where the sensitivity matrices (C) are, as in the orthogonal distance regression model, represented by the inverse of the squared combined ($u_i(c_5)$ and $u_\phi(c_5)$) uncertainty of each run. The one-dimensional uncertainty matrix (U) holds the correlated uncertainty component of each five-day run (u_ϕ (c_5)). As such, the size of the U-matrix depends on the number of successful five-day calibration runs that are available for a satellite. The correlation matrix (R) is two dimensional. As the error of the SRF reconstruction is fully correlated for the lifetime of a satellite, R is set to unity.

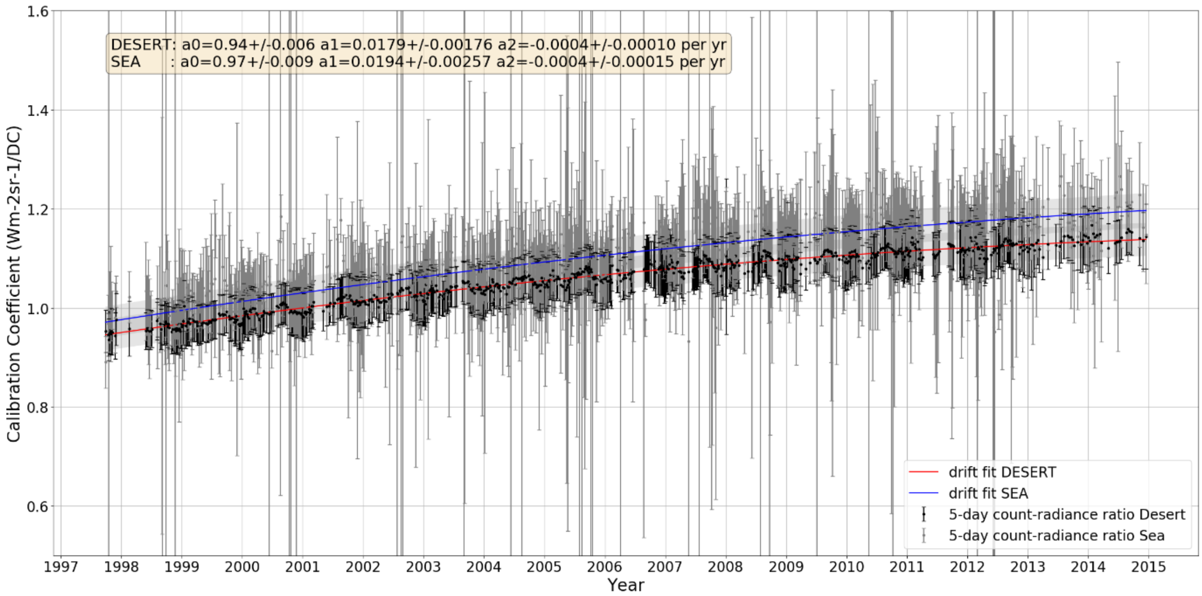

Figure 4: *Illustration of the polynomial fit and a_{cf} calculation for Meteosat-7. Each black dot represents a mean calibration coefficient from one 5-day calibration run above a desert site. The red line represents the polynomial fit through those data.*

Table 3: *Uncertainty components considered for each 5-day calibration run*

$u_m(c_5)$	Uncertainty of the radiative transfer model output (intrinsic 6S errors).
$u_p(c_5)$	Uncertainty of atmospheric and surface parameters used as input to the radiative transfer model
$u_\phi(c_5)$	Uncertainty due to errors of the spectral response function (RD 9).
$u_r(c_5)$	Uncertainty from random errors e.g. due to instrument noise.

4.2.3 Computation of Illumination Geometry

The computation of the illumination geometry, i.e. the solar zenith angle θ (SZA), is prone to add additional uncertainty in the conversion of radiances into the top of atmosphere bidirectional reflectance factor (BRF). In order to provide a dataset with traceable uncertainties, the SZA and the related uncertainty are included in the analysis of the FCDR. The algorithm applied for the generation of the FCDR follows the standard procedure for the illumination geometry at EUMETSAT. It is described in Eqs. (5-7):

$$\theta = \cos^{-1}(\sin(lat)\sin(\delta) + \cos(lat)\cos(\delta)\cos(\omega)) \qquad (5)$$

$$\omega = (t_S / 4) - 180 \qquad (6)$$

$$t_S = t - (EOT(t) - (4 * (-1 * lon))) \qquad (7)$$

where *lat* is the latitude, δ is the solar declination, and ω is the local hour angle (Eq. 6). The local hour angle (t_S) is computed from the solar time that depends on the longitude (*lon*) and the Equation Of Time (EOT), which describes the time difference between apparent solar time and mean solar time at that location (Eq. 7). The detailed subroutine in use for the computation, including the constant values that describe the curvature of the earth, are provided in Appendix A.

4.2.4 Filtering/Flagging of Invalid Images and Counts

This section presents six basic tests that the FCDR software performs for each pixel in the images. Pixels with invalid values are flagged. The six tests are performed separately, but the results is stored in a combined pixelwise bitmask.

Solar Zenith Angle

The computation of the bidirectional reflectance factor amplifies the signal for pixels with large SZA. This increases the signal to noise ratio. To avoid the usage of those measurements, SZA larger than 90° are flagged.

Suspicious Uncertainty

Earth count values below or equal to the dark signal should not occur. If they do, this indicates a potential issue with the computation the dark signal and thus also of the noise level. Count values below or equal to the dark signal are flagged.

Space corner check / dark signal

This check searches for suspicious patterns in the space corners for each detector. If the mean in one corner deviates from the mean of all space corners by more than the standard deviation, the dark signal of that space corner is flagged. Besides the flagging, also a mitigation of the problem is performed. That means the relevant dark signal provided in the FCDR is computed from the remaining space corner values or, if the number of remaining space corner values is below 10000, the space corner mean stored in the RECT2LP headers is used. In most cases only one of the space corner measurements is corrupted, and the flag can be ignored. Only users that require very robust dark signal estimates may care about this.

Pixel not on Earth

This flag is set during the computation of the geolocation. In case the observation is not located on Earth (the sensor was pointing to space) it is flagged.

Acquisition time

The accurate acquisition time can be estimated from a polynomial that is stored for each image line. It does not cover all pixels in a line. For pixels outside of the range of the polynomial, the time is approximated. When this is the case, the acquisition time flag is set.

Geolocation quality

The geolocation uncertainty is provided as a separate data layer. In some cases this uncertainty estimate may be suspicious. The geolocation quality flag is set in cases less than 5 landmarks were available for computing the statistics or when the standard deviation of the landmarks exceeds 1.5 pixel.

4.3 Uncertainty – Effect-wise Analysis

4.3.1 Overview over all uncertainty effects

The uncertainty analysis is performed by considering the different input quantities to the measurement equation. Each input quantity may be influenced by one or more error effects, of which each has an associated probability distribution. The aim is to establish the probability distribution of the output quantity [RD 6]. The uncertainty analysis performed for the MVIRI FCDR uses the following measurement equation:

$$\tilde{R} = \frac{\pi d^2}{\tilde{E}_{0,sun}\cos(\theta)}[(\overline{C}_E - \overline{C}_S)(a_0 + a_1 Y + a_2 Y^2)] \tag{8}$$

This equation is used to compute the top of atmosphere Bidirectional Reflectance Factor (BRF). As illustrated in Figure 5, many effects cause errors in the parameters of the measurement equation and subsequently in the calculated BRF. As the errors cannot be known in reality, they are described by uncertainties that can be thought of as probability distributions around the measured value. The most renown effects are the noise sources that impact the digital counts acquired by the instrument during Earth-views. Noise comes from the sensor electronics (like the amplifier), from the digitisation and from the Earth signal itself. As the error, that is caused by this effect, is different for each pixel, it can be considered independent. The same effects are also present while the sensors are pointing into deep space to determine the dark signal. As the dark signal is determined from the mean of all available space observations of an image, a good part of the noise averages out. This averaging for one image in turn has the effect that the error is present in all calibrated pixels of that image. The image navigation process in the ground segment also has residual errors in terms of the geolocation as well as the acquisition time. They affect the measurement as they create an error of the viewing geometry, particularly of the solar zenith angle. The SRF reconstruction approach and the vicarious calibration approach involve radiative transfer modelling for the selected calibration sites. Both approaches are susceptible to errors in the determination of the surface parameters, of the atmospheric parameters, of the solar spectrum, and of the model itself. SRF reconstruction and vicarious calibration both relate Earth counts ($\overline{C}_E$) to simulated radiances after subtracting the dark signal. Therefore, the dark signal measurement, approximated by the mean space count ($\overline{C}_S$) and it's error, as well as the noise level of the detection chains have an impact on the error of the reconstructed SRF and the vicarious calibration. The error of the reconstructed SRF propagates into: *i)* the convoluted effective solar irradiance and *ii)* the calibration coefficients. The following sections describe the effects of the different error sources, with the aim to develop an understanding of the error correlation patterns that are associated with them.

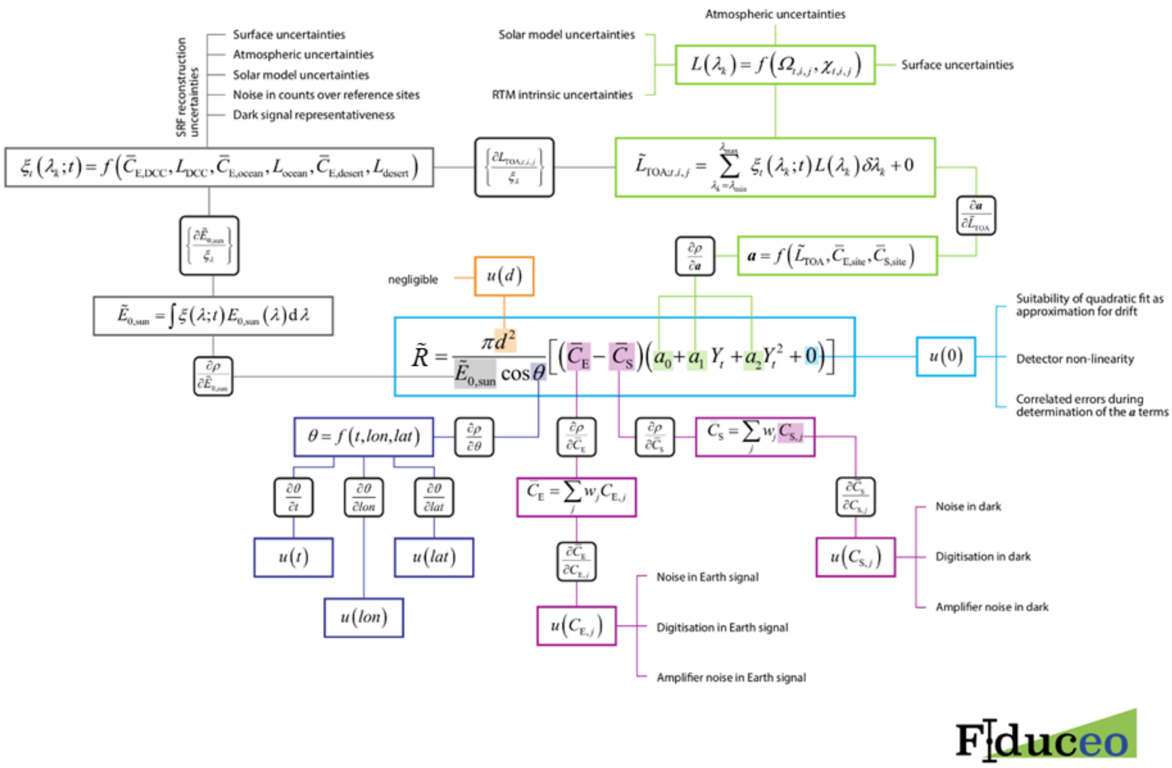

Figure 5: *Uncertainty diagram of the MVIRI reflectance measurements. In the centre of the diagram is the measurement equation. From there, branches reach out to the different effects that cause errors in each parameter of the measurement equation. The branches describe the transformation of the effect causing the error into the uncertainty of a parameter (e.g. averaging or application to a radiative transfer model). The black boxes represent the sensitivity coefficients that are used for the propagation.*

4.3.2 The uncertainty of the Earth counts

The uncertainty of the earth counts ($u_e(\bar{C}_E)$) is affected by the instrument noise. A measure of the noise level is obtained during the space view, where all observed variability is believed to originate from the instrument. The measure in use is the Allan deviation of the space observations. But due to some instrument characteristics it cannot directly be computed: Geo-rectified Earth counts contain the cubic-spline interpolated signal from a 4 x 4 block of Level 1.0 pixels from both visible detectors. The weighting of each detector is variable between pixels. In order to reflect the different noise levels of the detectors, the Allan deviation is computed for each detector individually and then combined together with the difference of the means of both detectors as depicted in equation 9.

$$u_e(\bar{C}_E) = \sqrt{\frac{1}{2}(\sigma_\tau(C_{S1})^2 + \sigma_\tau(C_{S2})^2) + \left(\frac{\bar{C}_{S1} - \bar{C}_{S2}}{2}\right)^2} \tag{9}$$

4.3.3 Digitisation Noise

The uncertainty caused by the digitisation ($u_d(\overline{C}_E)$) can be thought of as the standard deviation of a uniform distribution with the width of b digital counts as depicted in equation 10. For Meteosat-4 to Meteosat-7 b equals 1. Since Meteosat-1, -2 and -3 were encoded only on 6-bits but then inflated to the same 8-bits range as the other satellites, b of these early satellites equals 4.

$$u_d(\overline{C}_E) = \frac{b}{2\sqrt{3}} \tag{10}$$

4.3.4 The uncertainty of the dark signal offset (space count)

In the measurement equation, the dark signal is subtracted from the Earth counts in order to remove any variability in the offset of the detector current. The dark signal is estimated by averaging over a large number of space corner counts. The uncertainty of the dark signal offset ($u_d(\overline{C}_E)$) is smaller than the uncertainty of the Earth counts ($u_e(\overline{C}_E)$) because, in contrast to the the latter, uncertainty it averages out, and might be neglected. However, two assumptions have to be made that cause significant uncertainty: *a)* the two visible detectors have the same dark signal offset and it can be represented by a single value and *b)* the dark signal offset does not change during one scan. In reality, assumption *a)* is not true and the dark signal offset of the two detectors is different by up to more than one count. The uncertainty caused by this can be quantified by the standard deviation between the means of the two detectors as depicted in equation 11.1. Assumption *b)* is also not always valid, which becomes apparent in differing averages for the different space corners even for the same detector. To consider the resulting uncertainty, the standard deviation of the four space corner averages has to be considered as well (equation 11.2). The same evaluation needs to be done for both detectors individually (equation 11.3). The three above described effects can be combined into one single measure of the dark signal uncertainty according to equation 11.4.

$$u(\overline{C}_{S,d}) = \sqrt{\left((\overline{C}_{S1} - \overline{C}_S)^2 + (\overline{C}_{S2} - \overline{C}_S)^2\right)} \tag{11.1}$$

$$u(\overline{C}_{S,s1}) = \sqrt{\frac{\sum_{c=1}^{4}(\overline{C}_{S1}(c) - \overline{C}_{S1})^2}{3}} \tag{11.2}$$

$$u(\overline{C}_{S,s2}) = \sqrt{\frac{\sum_{c=1}^{4}(\overline{C}_{S2}(c) - \overline{C}_{S2})^2}{3}} \tag{11.3}$$

$$u(\overline{C}_S) = \sqrt{u(\overline{C}_{S,d})^2 + u(\overline{C}_{S,s1})^2 + u(\overline{C}_{S,s2})^2} \tag{11.4}$$

4.3.5 The calibration parameters a_0, a_1, a_2, and the "*+0*" term

As described in section 0, the independent components of the calibration uncertainties are covered in the covariance matrix that is determined from the residuals of the fitted calibration polynomial with the parameters a_0, a_1 and a_2. The fully correlated error of the SRF characterisation is not captured in these residuals, because it is present in every 5-day calibration run. As this error still introduces an unknown bias to the calibration coefficient, it has to be assigned to the $+0$ term as in equation 4.

4.3.6 Uncertainty of the Solar Irradiation

The uncertainty of the solar irradiation ($u(\tilde{E}_{0,sun})$) is computed from the covariance matrix of the reconstructed SRF as described in equation 12.

$$u(\tilde{E}_{0,sun}) = \int_{\lambda}\int_{\lambda'} E_{0,sun}(\lambda) S_{\phi}(\lambda,\lambda') E_{0,sun}(\lambda') d\lambda d\lambda' \tag{12}$$

4.3.7 Uncertainty of the Solar Zenith Angle

The uncertainty of the solar zenith angle ($u(\theta)$) is dominated by the uncertainty of the geolocation and of the acquisition time. As the precision of the acquisition time is within a second, the impact of acquisition time uncertainty on $u(\theta)$ can be neglected. The geolocation, particularly for poorly navigated images, can have a noticeable impact on $u(\theta)$. The geolocation accuracy is operationally determined in line ($u(l)$) and element ($u(e)$) directions using a set of 128 landmarks. The impact of the geolocation uncertainty onto the solar zenith angle is evaluated separately for latitudes ($u_{lat}(\theta)$) and longitudes ($u_{lon}(\theta)$) and then combined (Equation 13). For this purpose the sensitivity coefficients of the solar zenith angle for latitudes ($C_{\theta,lat}$) and longitudes ($C_{\theta,lon}$) are determined using Monte-Carlo methods. The change of latitude (∂lat) and longitude (∂lon) that corresponds to the uncertainties in line and element direction is determined for each pixel.

$$\begin{aligned} u_{lat}(\theta) &= C_{\theta,lat}\sqrt{\left(\frac{\partial lat}{u(l)}\right)^2 + \left(\frac{\partial lat}{u(e)}\right)^2} \\ u_{lon}(\theta) &= C_{\theta,lon}\sqrt{\left(\frac{\partial lon}{u(l)}\right)^2 + \left(\frac{\partial lon}{u(e)}\right)^2} \\ u(\theta) &= \sqrt{u_{lat}(\theta)^2 + u_{lon}(\theta)^2} \end{aligned} \tag{13}$$

4.3.8 Evaluation of Error Correlations among Effects

The spectral response function is used for the convolution of the solar irradiance and for the convolution of the simulated radiances in the calibration process. Both quantities thus contain the error that was made during the SRF reconstruction process; this error is partially correlated. Different to the simulated Earth spectra, the solar spectrum, due to its different shapes, emphasises different parts of the SRF. Another reason why the correlation is partial is the complex calibration procedure that involves additional processes that affect the uncertainties of the derived calibration parameters.

In the measurement equation, the calibrated radiance is divided by the convoluted solar irradiance. The correlated part of the error of both quantities cancels out during this process. An accurate determination of the correlation between the parameters is very important to correctly propagate the SRF uncertainties into the reflectance. Due to the complexity of the calibration process, the assessment of the correlations is only possible by iterating the calibration process in a Monte-Carlo simulation, using a representative ensemble of disturbed spectral response functions. The calibration process is similar to the nominal calibration run described in section 4.2.2. Iterating the calibration process is computationally very expensive, as it involves numerous radiative transfer simulations. Therefore, the number of ensemble members is limited to 15.

A key for the Monte Carlo simulation is the selection of the disturbed SRF ensemble. The realisation of the ensemble has to represent the covariance of the SRF error as function of wavelength. The procedure is implemented following [RD 24]. Broadly summarised, it involves the eigenvalue decomposition of the SRF covariance matrices that are multiplied with one standard normal distributed random vector for each ensemble member. To generate an ensemble of 15 representative realisations of the SRF, 15 normal distributed random vectors are required. An example of the derived SRF ensemble is provided in Figure 6, along with the observed error co-variability from the Monte-Carlo runs of the calibration system that were performed using those SRFs. The scatterplots illustrate the strong correlation between the error of the a_0 term (calibration factor at launch date) and the error in the solar irradiance. Weaker correlations are also present between errors of the a_1 term and the solar irradiance as well as between the a_0 and a_1 terms. The a_2 (non-linearity) term is not affected by the variability within the SRF ensemble.

The correlation matrix between the effects that is derived from the above results is provided in every fullFCDR file. In the easyFCDR, the combined structured uncertainty of the BRF is computed using this correlation matrix (Equation 15).

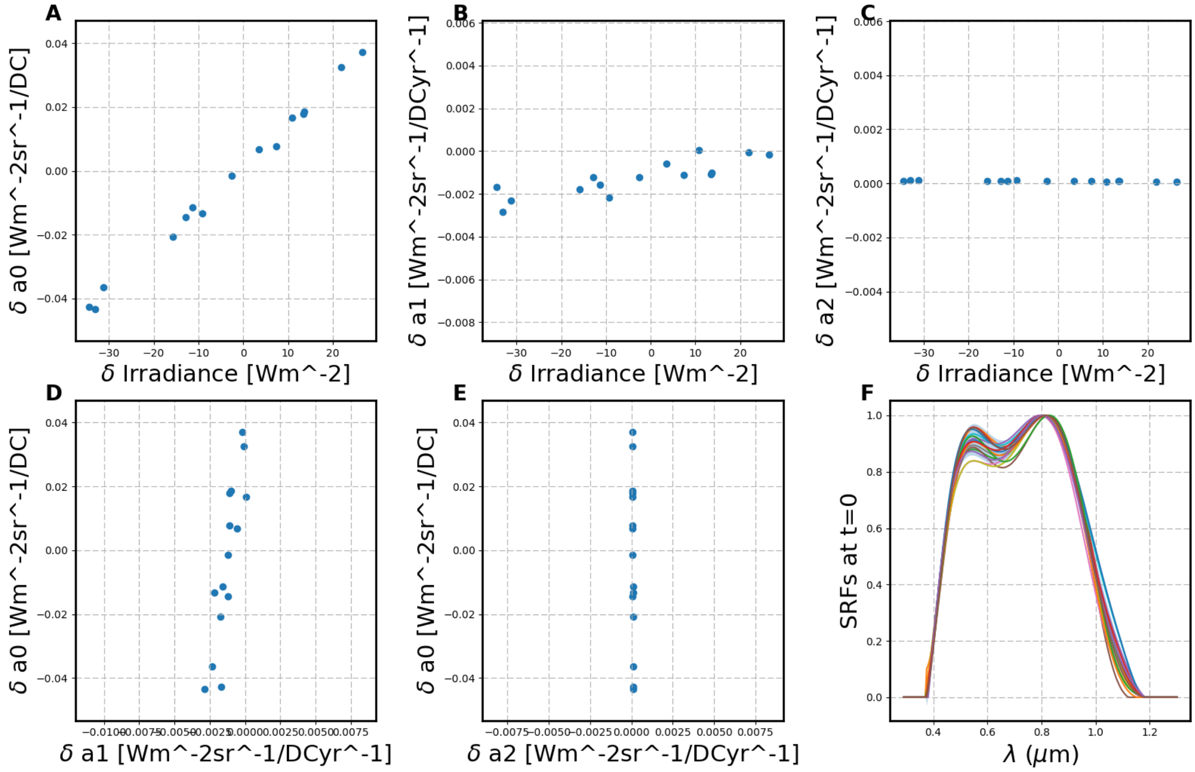

***Figure 6:** Co-deviations from the normal calibration of the solar irradiance with calibration parameters a0 (**A**), a1 (**B**) and a2 (**C**) as well as of a0 with a1 and a2 (**D** and **E**), when using a member of an ensemble of spectral response functions (**F**). The generation of the SRF ensemble considers the covariance matrix of the reconstructed SRF.*

4.4 Uncertainty – Combined Analysis

4.4.1 Combination of Independent Effects

Independent uncertainties of the reflectance ($u_i(\tilde{R})$) result from uncorrelated errors. In the MVIRI case, this is the combined electronics noise that is represented in equation 9 and the digitisation noise that is represented in equation 10. They propagate into a combined uncertainty of the reflectance according to equation 14 where they are multiplied with the first derivative of the measurement equation as the sensitivity coefficient.

$$u_i(\tilde{R}) = \sqrt{u\left(\bar{C}_{\mathrm{E,e}}\right)^2 + u\left(\bar{C}_{\mathrm{E,d}}\right)^2} * \frac{\partial \tilde{R}}{\partial \bar{C}_E} \tag{14}$$

4.4.2 Combination of Structured Effects

Structured uncertainties of the reflectance ($u_s(\tilde{R})$) result from spatially and/or temporally correlated errors. An extreme example is the calibration coefficient (a_{cf}, as defined in Equation 3) that is determined only once over the whole lifetime of a satellite. Any error made during the calibration process will thus be apparent in every BRF value derived from the instrument data. A more subtle example is the space count value ($\bar{C}_S$), which is determined only once per image. The error of the space count value is apparent in every derived BRF of the same full disk image, but it is independent from the error of the images before and after. Apart from spatial and temporal correlations, effects described by structured uncertainty can also be correlated with other effects. For example, both the uncertainty of the calibration coefficient (a_{cf}) as well as that of the solar irradiance ($\tilde{E}_{0,sun}$), are dominated by the uncertainty of the SRF. The correlation of the error between both quantities is therefore high. These errors were estimated by performing Monte Carlo calibration runs (Section 4.3.8) with an ensemble of perturbed SRFs. In order to account for the correlations, the structured uncertainties of the BRF are combined as:

$$u_s(\tilde{R}) = \sqrt{\sum_{s=1}^{n_s} c_s^2 u(x_s)^2 + 2\sum_{s=1}^{n_{s-1}} \sum_{s'=s+1}^{n_s} c_s c_{s'} u(x_s, x_{s'})} \tag{15}$$

where s is the index for structured effects $x_s = [a_0, a_1, a_2, +0, \tilde{E}_{0,sun}, \theta, C_S]$, c_s denotes the sensitivity coefficient for each effect, $u(x)$ is the uncertainty of an effect, and $u(x_s, x_{s'})$ is the covariance matrix for effects s and s'. Note that for the representation of the individual error covariance the recalibration coefficient is represented by the parameters of equation (3).

5 INFRARED AND WATER VAPOUR CALIBRATION ALGORITHM

5.1 Overview

In this section, the algorithm for the recalibration of the infrared and water vapour channel (or band) measurements of MVIRI onboard MFG satellites is presented, using the Multi Sensor Infrared Channel Calibration (MSICC) algorithm [RD 32]. The generic nature of the MSICC algorithm allows it to be applied to any other similar geostationary satellite measurements. Because historical geostationary imagers did not have onboard calibration devices, one needs to rely on vicarious methods that recalibrate radiances from an instrument (also referred to as the monitored instrument) with radiances from superior instruments operated on another satellite or on an aircraft (also referred to as the reference instrument) using matchups of geostationary and reference measurements. Comparing matched-up observations of a monitored and a reference instrument enables a quantitative estimate of the bias between both instruments. The measurements from the reference instrument, which are superior to the accuracy of the monitored instrument, can be used to recalibrate the monitored instrument taking into account differences in instrument spectral response and spatial resolution, as well as temporal and spatial uncertainties of the matchups. The measurements of the reference instrument need to be representative for the IR and WV channels of the MVIRI instrument (the monitored instrument), and they need to span the entire period that the MVIRI instruments were/are operated. In this section more details is given on the procedure for selecting suitable reference instruments, as well as details of these instruments. The MSICC algorithm is based on generic principles to ensure traceability, and follows the following hierarchical approach:

1) Selecting reference instruments;
2) Adjusting for spectral band differences;
3) Co-locating measurements from monitored and reference instruments;
4) Computing of recalibration coefficients;
5) Anchoring recalibration coefficients to a prime reference.

5.2 Reference satellite observations

This section describes the main characteristics of the reference instruments. Observations of three types of reference instruments are used for the recalibration, they are the Infrared Atmospheric Sounding Interferometer (IASI), the Atmospheric Infrared Sounder (AIRS), and the High Resolution Infrared Sounder (HIRS).

The IASI instrument is a Michelson interferometer covering the infrared spectral domain from 645 to 2760 cm^{-1} (3.62–15.5 μm). The IASI measurements are aimed to generate high-resolution atmospheric sounding, with an accuracy requirement of 1 K for tropospheric temperature and 10% for humidity for a vertical resolution of 2 km, and the retrieval of trace gas total column amounts. IASI is a cross-track scanner, with 30 fields of regard (FOR) per scan. Each FOR measures a 2 × 2 array of footprints, each of which has a 12-km diameter at nadir. The spectrum is measured in three wavelength bands (645–1,210, 1,210–2,000, and 2,000–2,760 cm^{-1}), each of which has a separate detector, allowing the continuous spectral coverage with no gaps. The raw measurement made by the instrument is an interferogram that is processed into a radiometrically-calibrated spectrum on board the satellite using two calibration views. Further processing by the terrestrial data reception centre delivers calibrated radiances (known as the level 1c product) to the end user. The radiances consist of 8,461 spectral samples (commonly referred to as "channels") every 0.25 cm^{-1} wavenumbers, with a spectral resolution of 0.5 cm^{-1} (full width at half maximum) after apodisation. More details are given in Hilton et al. [RD 22]. The IASI level 1c product is used for the recalibration of the MVIRI instruments.

The AIRS instrument, when developed, incorporated numerous advances in infrared sensing technology to achieve a high level of measurement sensitivity, precision, and accuracy providing 2378 spectral samples (channels), all measured simultaneously in time and space. AIRS looks towards the ground through a cross-track rotary scan mirror which provides ± 49.5 degrees (from nadir) ground coverage along with views to cold space and to on-board spectral and radiometric calibration sources every scan cycle. The scan cycle repeats every 8/3 seconds. Ninety ground footprints are observed each scan. One spectrum with all 2378 spectral samples is obtained for each footprint. The AIRS IR spatial resolution is 13.5 km at nadir from the 705.3 km orbit. The data are available from late August 2002 till today. The spectral range of the MVIRI IR window channel is covered almost completely with two small gaps., However, there are large spectral gaps in the MVIRI WV channel spectral coverage. Most gaps in AIRS data are caused by the instrument design and some small gaps are due to bad detectors, which can easily be filtered out with quality information provided as part of the meta data. Small gaps from bad detectors do not significantly affect the comparison to a broadband instrument because relatively little information is lost. We used AIRS v5 level 1b data for the recalibration of the MVIRI instruments..

The HIRS instrument is a 20-channel infrared scanning radiometer designed for atmospheric sounding. Among the twenty spectral channels, there are twelve long-wave channels (669 to 1529 cm^{-1}), seven shortwave channels (2188 to 2657 cm^{-1}), and one visible channel (0.69 μm), all of which use a single telescope with a rotating filter wheel consisting of twenty individual spectral filters. An elliptical scan mirror is stepped 56 times in increments of 1.8 degrees to provide scanning across the track. The field of view for HIRS long-wave channels is 1.4 degrees which corresponds to a foot-print size at the ground at nadir of 20.3 km. We used operational HIRS data obtained from the NOAA CLASS archive to recalibrate the MVIRI instruments. Though HIRS measurements are not hyperspectral, their radiometric quality is superior to MVIRI measurements due to the use of on-board calibration targets and thus qualify as reference measurements.

The HIRS instruments were subject to a significant spectral design change in the channel 12 between HIRS/2 and HIRS/3/4 as shown in Figure 7. This channel spectrally matches the MVIRI WV channel and is important for the recalibration. ,. The impact of this change has been analysed using a month of co-locations between HIRS/2 and HIRS/3 data with Meteosat-7 data and the results are shown in Figure 8. From HIRS/2 to HIRS/3 the change is not only the shift in the central wave number, but also the width of the SRF has been reduced. This leads to a more uncertain fit between HIRS radiances and Meteosat-7 radiances, the uncertainty has tripled from 0.115 to 0.339 mW/m2/sr/cm^{-1} and the correlation has gone down from 1.00 to 0.96. This implies that the use of HIRS/3/4 is not suitable for recalibrating the WV channel of

MVIRI. Figure 8 also shows saturated pixels at high radiance for Meteosat-7, which were removed from processing by filtering out MVIRI pixels with zero standard deviation in a 3 × 3-pixel area.

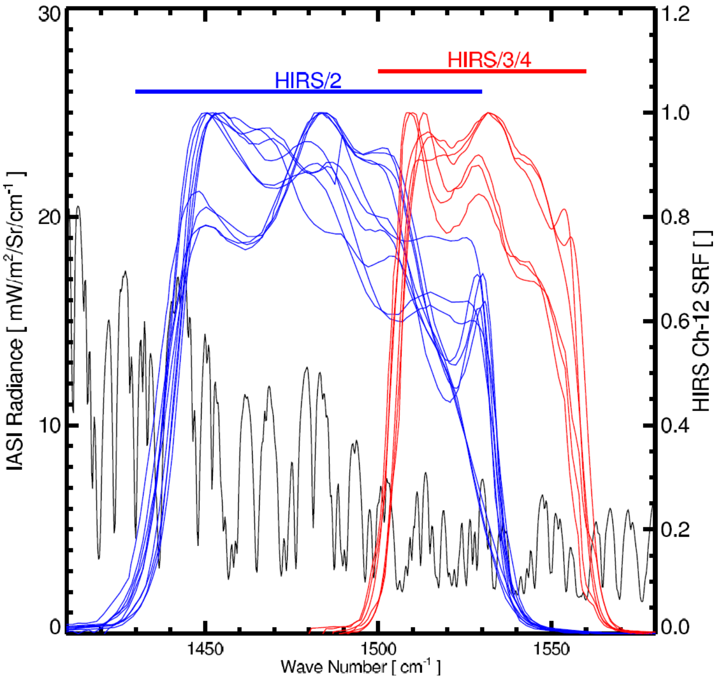

Figure 7: *Spectral Response Functions of HIRS/2 (blue), HIRS/3 (red) and HIRS/4 (red) instruments for the Channel 12 (~6 µm). IASI spectra (black) are also shown to illustrate atmospheric opaqueness at these spectral regime. The approximate spectral ranges for the HIRS/2 series and the HIRS/3 and HIRS/4 series are marked at the top, which clearly indicates a spectral shift between the generations. Satellites carrying HIRS/2 instruments are TIROS-N and NOAA-6 through NOAA-14. Satellites carrying HIRS/3 instruments are NOAA-15 through NOAA-17. Satellites carrying HIRS/4 instruments are NOAA-18, NOAA-19, Metop-A, and Metop-B.*

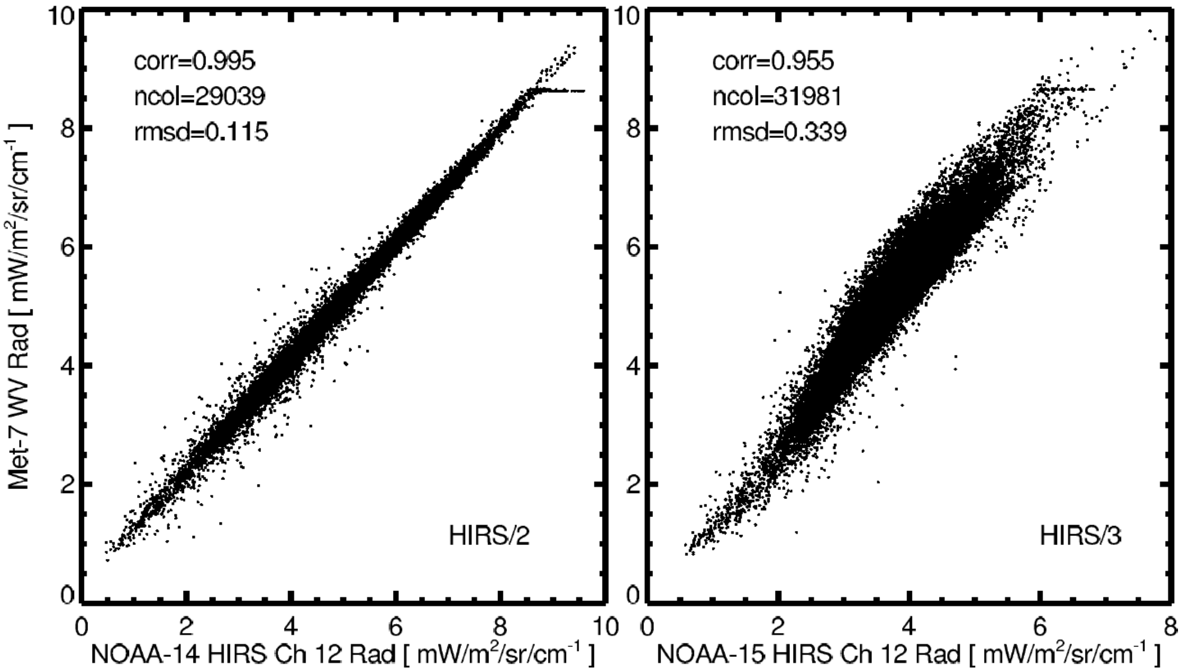

Figure 8: *Impact of Channel 12 SRF changes between HIRS/2 and HIRS/3/4 on the collocation uncertainties with MVIRI WV channel. Collocations are for January 2003.*

The last HIRS/2 instrument operated on NOAA-14 provided good quality data till early 2006, which implies there is a gap in available reference data between HIRS/2 and the first IASI instrument onboard Metop-A, which became operational by mid-2007. Thus, it was decided to use the hyperspectral measurements of the AIRS instrument onboard National Aeronautics and Space Administration (NASA)'s Aqua satellite to serve as another reference.

Two issues need to be addressed before using the AIRS data as reference measurements. Firstly, as described above the observations of the AIRS instrument are subject to permanent spectral gaps, in particular within the broad MVIRI WV channel. The impact of this on the computation of recalibration coefficients needs to be tested. Secondly, the AIRS Test and Calibration Facility evaluations showed that the output, the raw digital number (dN), observed for successive space views for each detector is predictable to an accuracy approaching the Gaussian noise for most detectors. For some detectors, some kind of non-Gaussian excursion in the noise have detected and this is referred as a "pop" or "popcorn noise". The number of "pops" observed during each six-minute interval is counted and reported as pops/minute in the QA report of the 6 minutes granule of the AIRS files. The data for the entire scan line of the detector where the "pop" was detected are be flagged as radiometrically bad and cannot be used as a reference measurement. Popping is observed for about 60 out of the 2378 channels and these channels are varying over time. In order to use AIRS as reference the permanent gaps and popped channels need to be understood and corrected for.

5.3 Spectral band adjustment

In this step, co-located data are transformed to allow their direct comparison. This includes modifying the spectral characteristics of the reference observations so that they can be directly compared with the monitored instrument's measurements. This requires knowledge of the instruments' spectral characteristics, i.e., the spectral response functions. The outputs of this step are the reference radiances (spectra in case of AIRS or IASI and broadband radiance in case of HIRS/2) to the best estimates of monitored radiances, together with uncertainties associated with this transformation.

5.3.1 Spectral band adjustment for IASI

The measurements for the IASI hyperspectral sounder instrument do not contain spectral gaps in the spectral range of the monitored instruments, i.e., IASI has full spectral coverage for the IR and WV channels onboard the EUMETSAT geostationary satellites. Therefore, the reference radiance of a particular channel of the monitored instrument can be directly calculated by convolving the IASI spectra with the SRF of that channel.

5.3.2 Spectral band adjustment for AIRS

Before using AIRS spectra, checks for bad data are performed using the quality flags that are provided with the data. AIRS channels having nonzero "CalChanSummary" flag value are excluded. A flag value of zero means the channel was well calibrated for all scanlines in an AIRS 6 minutes granule as such a channel is referred below as a "good AIRS channel". "CalChanSummary" flag identifies calibration performance for each channel over the whole granule.

The spectral gaps and popped channels, as discussed above, pose a significant problem for using of AIRS spectra as reference for recalibrating MVIRI IR and WV channel measurements. The methods described in the literature for filling the gaps in the AIRS data use simulated measurements for the gaps and compromised channels taking model profiles including clouds as simulation input (see for example, [RD 26]). However, these methods, especially in the presence of clouds, are subject to significant uncertainties. Therefore, we decided to develop a methodology to compensate for the gaps and compromised channels, using IASI spectra instead of simulated spectra. Our methodology can be broken down into three steps:

1) To simulate broadband measurements of MVIRI IR and WV channels with IASI spectra. In order to make sure the full atmospheric variability is captured about 200 thousand IASI spectra of randomly selected orbits (one per month) for a full year, i.e., 12 orbits were collected. . In addition, AIRS radiances are simulated by convolving the IASI spectra with AIRS channel SRFs;
2) To determine predictors that vary from granule to granule, which are used to compute the simulated broadband radiances of MVIRI IR and WV channels of the simulated "good AIRS channel" radiances (~260 channels in the IR band and ~210 channels in WV band) using multiple linear regression;

3) To produce predictions of the broadband radiances of MVIRI IR and WV channels using real AIRS spectra by applying the predictors determined in step 2.

Figure 9 demonstrates the robustness of the above-described methodology, which reveals a very low root mean square difference (RMSD) between the broadband radiances computed from IASI measurements and those from real AIRS measurements. The uncertainty of this methodology is about an order of magnitude less than the values reported in [RD 26].

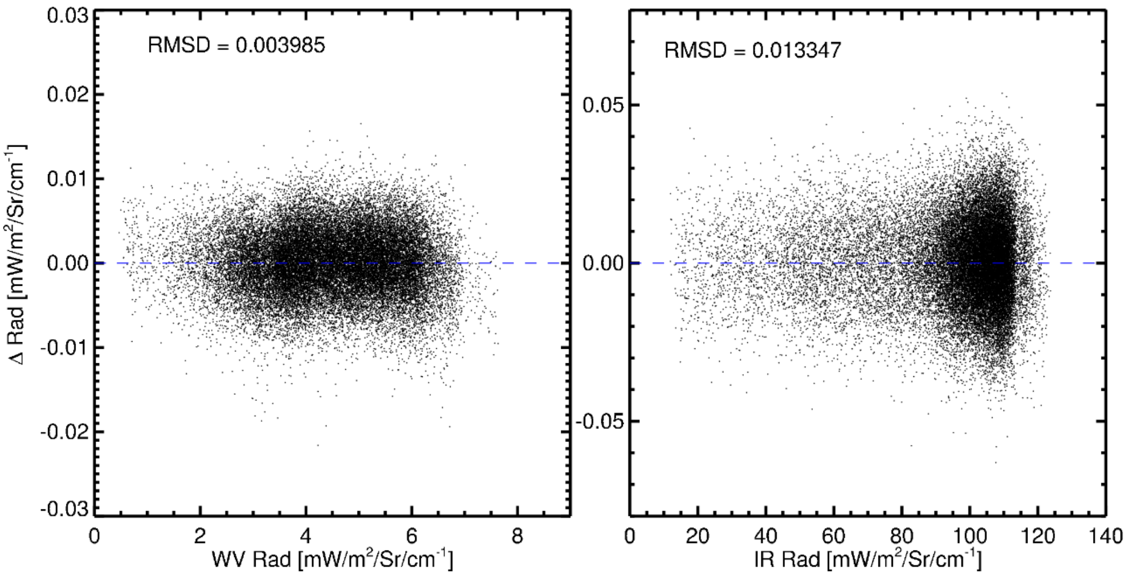

Figure 9: *Demonstration of constructing broadband radiances from available AIRS channels. The plots show the difference between the Meteosat-7 radiances computed from available AIRS channels and from the full IASI spectra for the WV (left) and IR (right) channels as function of MVIRI channel radiance.*

5.3.3 Spectral band adjustment for HIRS

The spectral conversion of broadband radiances provided by instruments, such as HIRS, is not trivial. A traditional way of computing the conversion factors or spectral band adjustment factors (SBAFs) is to use simulated radiances from an atmospheric profile dataset by using a radiative transfer model [RD 33]. There are two main shortcomings in this approach: 1) the profile dataset may not capture the real atmospheric variability and 2) the radiative transfer model is not able to simulate the actual radiances especially in the presence of clouds.

One way to overcome this is to use hyperspectral measurements, such as IASI spectra that have a spectral resolution of 0.25 cm^{-1}, to simulate both reference and monitored broadband radiances by convoluting the spectra with respective SRFs. In order to make sure the full atmospheric variability is captured the same set of IASI spectra as for the AIRS adjustment is used. These spectra are convolved with SRFs of the monitored instrument and reference instrument to obtain simulated radiances. An example of deriving SBAF is shown in Figure 10, which shows a very robust linear relationship between NOAA-14 HIRS/2 channel 8 and

12 radiances and Meteosat-7 IR or WV channel radiances (both simulated from IASI spectra). The red line in the figure shows the linear fit and the root mean square of the fit residual is 0.6 mW/m^2/sr/cm^{-1} for the IR channel and 0.02 mW/m^2/sr/cm^{-1}for the WV channel. The small root mean square difference (RMSD) values suggest that uncertainties in the fit parameters are very small. The uncertainties of the offset and slope are 0.00687 and 0.00007 for the IR channel and 0.00031 and 0.00005 for the WV channel in this case. As evident in WV channel radiances the monitored and reference radiances can have significant differences due to differences in SRFs and they need to be spectrally adjusted. SBAFs are computed for all possible monitored and reference satellite combinations and are used to convert HIRS radiances to equivalent Meteosat IR or WV channel radiances.

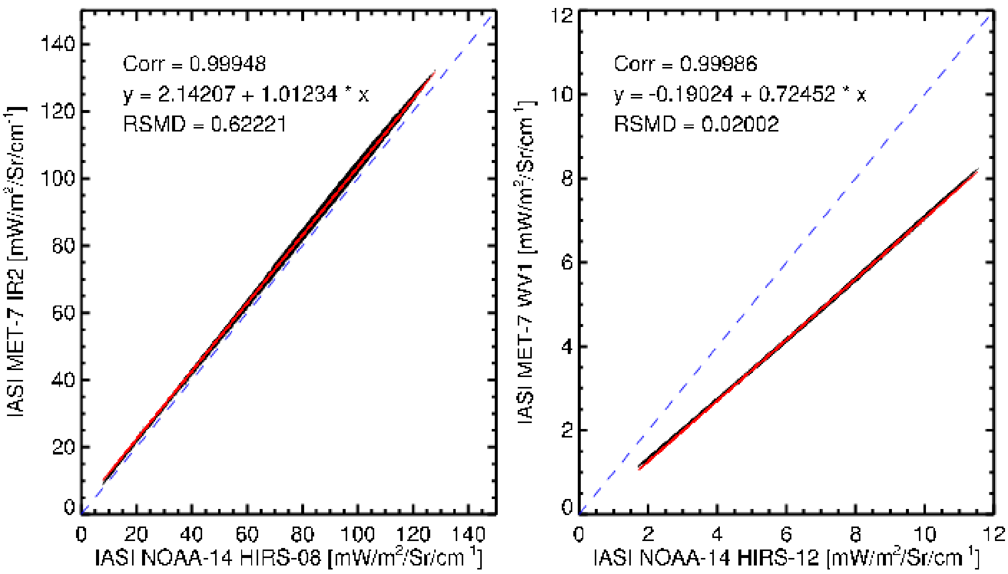

Figure 10: *Derived Spectral Band Adjustment Factors (SBAF) for the IASI spectra data set containing 202477 spectra. The resulting robust linear fit between the two radiances is denoted by the red line in each plot.*

5.4 Finding co-locations between reference and monitored measurements

The recalibration of MVIRI measurements is based on the comparison of the measurements (monitored measurements) to reference measurements of other satellite instruments. To facilitate such a comparison both measurements would ideally be taken at the same time and sampling the same spatial area with the same viewing geometry. This is not possible in reality because of they are flying on different platforms. Data from different instruments need to be co-located by applying thresholds, which define the maximum allowed differences in time, space, and for viewing conditions between the monitored and reference measurements. Co-locating the measurements using the thresholds, pairs of measurements of reference (REF) and monitored (MON) instrument data, which have similar geographical, temporal and geometrical attributes are created.. The co-locations are found using an in-house developed algorithm, which is described in detail in [RD 30]. A set of observations from a pair of instruments within a common period (e.g. a day or a month) is required as input to the co-location algorithm. The algorithm involves the following steps:

1. obtain data from both REF and MON instruments
2. select the relevant comparable portions and identify the pixels that are:
    a. spatially collocated,
    b. temporally concurrent,
    c. geometrically aligned, and
    d. spectrally compatible
3. calculate the mean and variance of these counts or radiances.

5.4.1 Co-location in Space

A target area is defined to be a little larger than the Field of View (FoV) of the reference instrument. Thus, it covers all the contributing radiation also considering small navigation errors, while being large enough to ensure reliable statistics of the variance of the radiances. Although the exact ratio of the target area to the FoV is instrument-specific, it ranges in general between 1 and 3 times the FoV, with a minimum covering 9 monitored instrument pixels.

For example, the MVIRI FoV is defined as squared pixels with dimensions of 5x5km^2 at Sub Satellite Point (SSP). An array of 3x3 MVIRI pixels centred on the pixel closest to centre of each reference pixel are taken to represent the co-location target area corresponding to the reference FoV. Also 5x5 MVIRI pixels' statistics are kept in the output, which can be used for additional assessment of the variability.

5.4.2 Co-location in Time

Time stamps of the spatially co-located monitored geostationary (GEO) satellite measurements and reference Low Earth Orbit (LEO) measurements are compared. If the time difference (Δt) between the overpass time of the LEO (t_{LEO}) and the GEO (t_{GEO}) satellites is greater than a maximum threshold (t_{max}) of 900s, the co-location is rejected, otherwise it is retained for further processing, that is:

$$\Delta t = |t_{LEO} - t_{GEO}| < t_{max} \tag{16}$$

5.4.3 Co-location in Viewing Geometry

The next step is to ensure that the spatially and temporally co-located measurements were observed under comparable geometrical conditions. This means they should be aligned such that they view the surface through similar atmospheric paths at similar incidence angles, including azimuth, polarisation as well as elevation angles.

Each pixel pair is tested sequentially to check whether the viewing geometries of the observations of both instruments were sufficiently close. The criterion for zenith angle is defined in terms of atmospheric path length, according to the difference in the secant of the observations' zenith angles. If these are less than pre-determined thresholds, the co-located pixels are considered to be aligned in viewing geometry and included in further analysis.

Otherwise, they are rejected. The geometric alignment of thermal infrared channels depends only on the zenith angle difference ($\Delta\theta$) and not azimuth or polarisation, and is accepted when:

$$\Delta\theta = \left|\frac{cos(\theta_{GEO})}{cos(\theta_{LEO})} - 1\right| < \theta_{max} \tag{17}$$

where θ is the satellite viewing zenith angle. The threshold value for θ_{max} can be quite large for window channels (e.g., 0.05 the IR channel), but must be rather small for more absorptive channels (e.g., < 0.02 for WV channel). However, unless there are particular needs to increase the sample size for window channels, a common θ_{max} value of 0.01 may be used for all channels. For co-locations between GEO and LEO satellites, this results in co-located measurements that are distributed approximately symmetrically around the equator, mapping out a characteristic slanted hourglass pattern. We limit the maximum incidence angle to 35° because it was observed that co-locations with larger incidence angles introduce more noise.

5.5 Determination of recalibration coefficients

The recalibration coefficients are computed on a daily basis, by collating five days of co-locations, two days before, the day in question, and two days after. The coefficients are computed by regressing the measured counts of the monitored instrument (DN; Digital Number) with co-located and spectrally adjusted radiances of the reference instrument. An example for co-location data for five days is depicted in Figure 11. The x-axis represent average (3x3 pixels) monitored counts and the y-axis represent the spectrally adjusted reference radiances. Each data point has uncertainties in both (x and y) axis directions. The uncertainties in the x axis direction are defined by the variance of the 3x3 pixels monitored counts. The uncertainties in the y axis direction are a combination of uncertainties of the reference measurements (pre-launch determined noise equivalent radiance) and uncertainties of the spectral adjustment. The linear regression uses the method described in Press et al [RD 27] which takes into account errors in both x and y and therefore those co-locations occurring under inhomogeneous conditions, represented by larger variance in the counts, get a smaller weight in the computation of calibration coefficients.

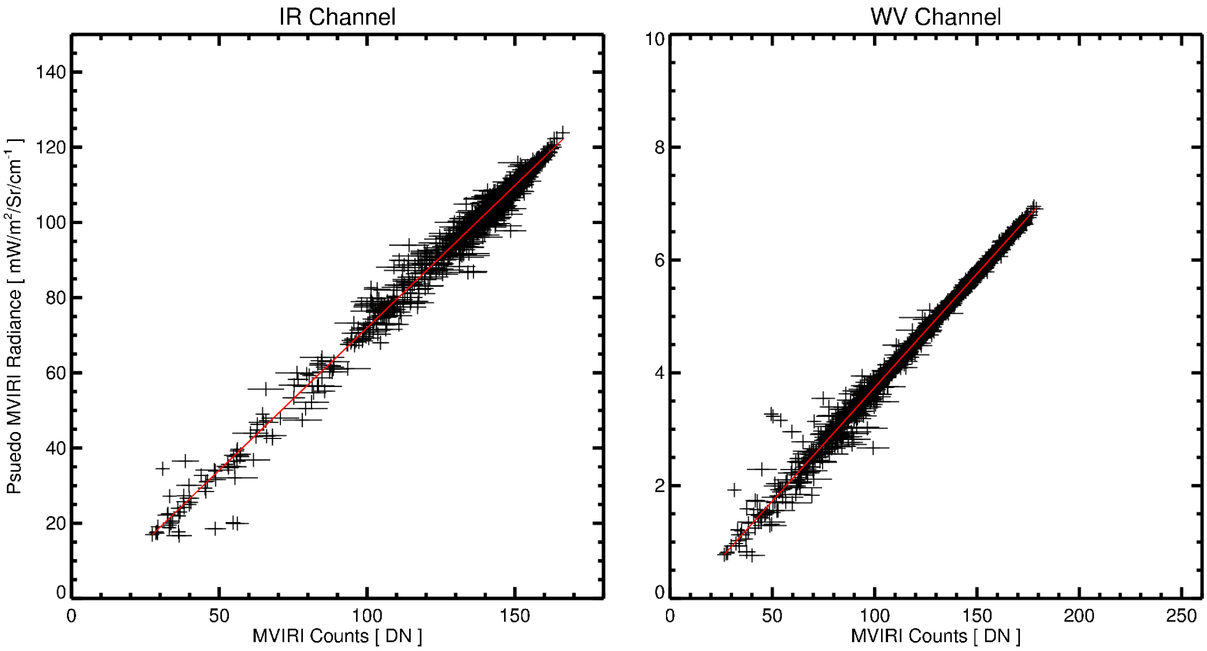

Figure 11: *Regression to compute the recalibration coefficients between MVIRI measured counts and MVIRI radiances computed from co-located spectrally convolved IASI spectra for the MVIRI IR channel (left) and for the WV channel (right). Errors in both the counts and convolved IASI radiances are used to compute the linear fit (red line) parameters. Calibration coefficients are computed per day by collating 5 days of matchups (+-2 days around the day for the calibration is performed).*

The calibration coefficients (offset, slope, and their corresponding uncertainties) are computed on a daily basis. From the black dots in Figure 12 it can be seen that day-to-day variations can be relatively large. These variations are caused mainly by varying representativeness of the co-locations to characterise the actual calibration of the instrument. To mitigate the effect of the day-to-day variations, we have smoothed the parameters so that they represent gross changes in the calibration parameters between two radiometric events. The smoothing is achieved using a boxcar smoothing function of five days wide. If the neighbourhood around a point includes a point outside the array, a mirrored edge point is used to compute the smoothed result. For example, when smoothing an n-element vector with a five-point-wide smoothing window, the second point of the result is equal to (A1+A0+A0+A1+A2)/5. These radiometric events (shown as dashed vertical lines in Figure 12 are gain setting changes of Meteosat-7 IR Channel.

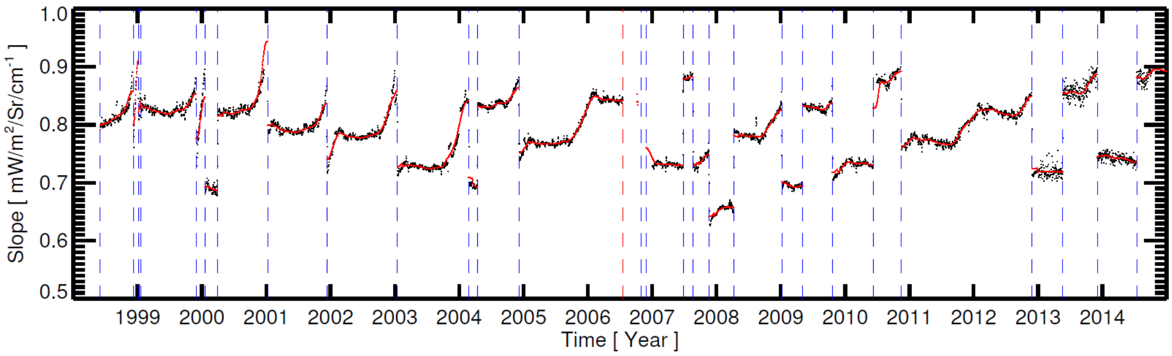

Figure 12: *Time series of calibration slope parameter for the Meteosat-7 IR channel. Vertical dashed lines represent radiometric events such as gain changes. The vertical dashed red line shows the start of the satellite's move to Indian Ocean. Black dotted lines represent daily calibration values and the red lines are the smoothed calibration values which are used for the recalibration.*

Recalibrated radiances for the IR (*L_ir*) and WV (*L_wv*) channels in mW/m2/sr/cm^{-1} can be obtained according to equations (18) and (19):

$$L\_ir = a\_ir + b\_ir * Count\_ir \quad (18)$$

$$L\_wv = a\_wv + b\_wv * Count\_wv \quad (19)$$

where *a_ir* and *a_wv* are the calibration offsets and *b_ir* and *b_wv* are the calibration slopes of the IR and WV channel respectively. The uncertainty in the recalibrated radiance due to recalibration procedure can be expressed as:

$$u(L) = SQRT(\sigma^2{}_a + \sigma^2{}_b * count^2) \quad (20)$$

where σ_a and σ_b are the uncertainties of the linear fit parameters.

5.6 Anchoring recalibration coefficients to a prime reference

The recalibration coefficients computed above may introduce systematic differences in the geostationary radiances due to systematic differences in the reference measurements and this may vary from one satellite to the other. In order to remove the inter-satellite biases in the reference measurements, all reference satellite measurements are anchored to a prime reference satellite using monitored measurements as bridges. Consider a_1 and b_1 as the offset and slope determined for a geostationary satellite using measurements of reference satellite 1 and a_2 and b_2 as the offset and slope determined for a geostationary satellite using measurements of reference satellite 2. Recalibrated radiance corresponding to the geostationary measured counts (*Count*) can be obtained as:

$$L_1 = a_1 + b_1 * Count \quad (21)$$

$$L_2 = a_2 + b_2 * Count. \quad (22)$$

Ideally, L_1 and L_2 are the same, but due to the potential bias in the reference measurements, L_1 and L_2 are not the same and the difference between the two can be approximated as the bias between the two reference measurements, assuming that the geostationary measurements do not have diurnally varying biases. If we assume satellite 1 as the prime reference, L_2 can be prime corrected as follows:

$$L^{1'}_2 = a^{1'}_2 + b^{1'}_2 * L_2 \tag{23}$$

where the prime correction coefficients $a^{1'}_2$ and $b^{1'}_2$ are obtained by linear regression using L_1 as independent variable and L_2 as dependent variable by accumulating data for a common period where both satellite 1 and satellite 2 can be matched up against the same geostationary satellite. Here we assume that the biases of the individual satellites are time invariant, which may not be valid for all cases. One can also analytically determine the offset and slope of the prime correction as follows:

$$b^{1'}_2 = b_1/b_2 \tag{24}$$

$$a^{1'}_2 = a_1 - a_2 * b^{1'}_2 \tag{25}$$

The concept of prime correction is demonstrated below using Aqua/AIRS, NOAA14/HIRS2 and Meteosat-7 as reference satellite 1, reference satellite 2 and the bridge geo stationary satellite, respectively. The NOAA14/HIRS2 and Aqua/AIRS were in operation during the whole period shown in Figure 13 except for a short period from the end of October 2003 to mid-November 2003 to avoid possible damage from a large solar flare. The black line and the red line in Figure 13 represent the recalibrated brightness temperature of Meteosat-7 WV channel based on NOAA14/HIRS2 and Aqua/AIRS, respectively. There is systematic difference between those two recalibrated radiances. For validation of the prime correction method, the parameters ($a_{n14pAqua}$ and $b_{n14pAqua}$) were estimated by using only a tiny fraction of the overlap period (highlighted by green colour). Those parameters were applied to whole period of WV channel radiance based on NOAA14/HIRS2, shown by the blue line in Figure 13.

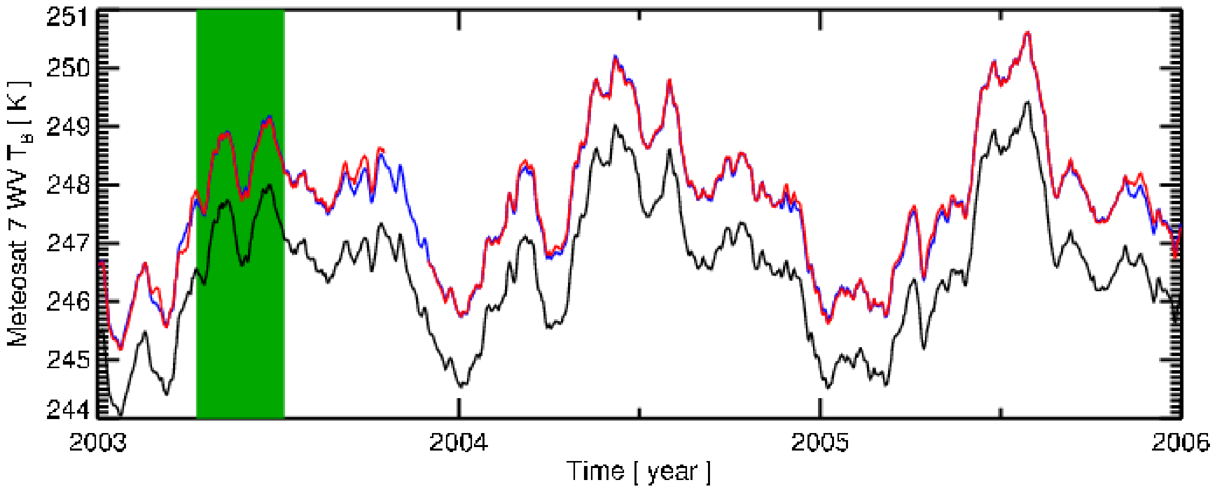

Figure 13: *Recalibrated brightness temperature of Meteosat-7 WV channel derived from recalibration coefficients by Aqua/AIRS (red) and those by NOAA-14/HIRS2 (black) and the prime corrected NOAA-14/HIRS2 (blue) using Aqua/AIRS as prime satellite. The green shaded region represent the period where data was used to compute prime correction. The AIRS instrument was placed in a safe mode from the end of October 2003 to mid-November 2003 to avoid possible damage from a large solar flare.*

The prime correction method was also tested by using two different geostationary satellites as bridges, this time we used Meteosat-5 and Meteosat-7 to compute prime correct NOAA-14/HIRS2 using Aqua/AIRS as prime satellite. Prime corrected radiance corresponding to a radiance value of 5 mW/m2/sr/cm-1 is 5.19±0.01 using Meteosat-5 and 5.21±0.01 using Meteosat-7, which are consistent with each other in statistical sense.

Prime corrections can be taken back in time for a series of reference instruments using different or same geostationary satellites as bridges. For example, radiances of satellite 3 can be prime corrected to satellite 1 by prime correcting radiance of satellite 2 to satellite 1 and then prime correcting satellite 3 radiances to satellite 2. That means,

$$L^{1'}{}_{3} = a^{1'}{}_{2} + b^{1'}{}_{2} * (a^{2'}{}_{3} + b^{2'}{}_{3} * L_{3}), \tag{26}$$

and it can be repeated for n number of satellites to prime correct n^{th} satellite to the prime satellite 1. Metop-A/IASI is considered as “prime reference” and all other measurements will be anchored to the prime reference measurements.

6 ASSUMPTIONS AND LIMITATIONS

Specific expected algorithm limitations are:

- For IR channels, co-locations with reference measurements were made without considering ray tracing. The effect of this is assumed to be negligible because on average the same atmosphere is observed by both instruments;
- For IR channels, the FIDUCEO metrorological approach is not applied and hence there are no uncertainty estimates provided with the data;
- For VIS channel calibration, only desert targets are currently used; the combined use of desert, ocean, deep convective clouds (DCC), and moon might improve the accuracy;
- For the VIS channel, uncertainty budget the solar spectrum has been assumed to have no uncertainty. The impact of this on the reflectance is small as the error cancels out. However, the inclusion of a more sophisticated solar model with uncertainties is recommended for future releases;
- An uncertainty introduced by the interpolation of the two MVIRI detectors during rectification has already been considered. However, for future releases of the data it is planned to perform the calibration on a detector level, which will reduce the uncertainty.
- For VIS channel calibration, the radiative transfer model used to simulate the radiances is not the state-of-the-art. It has known issues for example regarding the coupling between surface and atmosphere, atmospheric scattering and polarisation.

7 REFERENCES

Number	*Document Name*	*Reference*
RD 1.	Validation Report - MVIRI FCDR Release 1	EUM/OPS/DOC/18/990949
RD 2.	Product User Guide - MVIRI FCDR Release 1	EUM/USC/DOC/17/906121
RD 3.	GCOS-154, 2011: Systematic Observation Requirements for Satellite-Based Products for Climate, 2011 Update, December 2011, 139 pp.	
RD 4.	WMO webpage: http://www.wmo.int/pages/prog/sat/dataandproducts_en.php (assessed on 6 December 2018)	
RD 5.	ERA-CLIM2 European Union's Seventh Framework Programme (FP7; Grant Agreement No. 607029 (2014). http://cordis.europa.eu/project/rcn/188832_en.html (accessed on 6 December 2018)	
RD 6.	Merchant, C.J.; Holl, G.; Mittaz, J.P.D.; Woolliams, E.R. Radiance Uncertainty Characterisation to Facilitate Climate Data Record Creation. Remote Sens. 2019, 11, 474.	
RD 7.	Jonathan Mittaz Christopher J. Merchant and Emma R. Woolliams 2019: Applying principles of metrology to historical Earth observations from satellites. *Metrologia* 56 032002.	
RD 8.	Schulz, J., Albert, P., Behr, H.-D., et al. 2009: Operational climate monitoring from space: The EUMETSAT Satellite Application Facility on Climate Monitoring (CMSAF), 2009. *Atmos. Chem. Phys.*, 9, 1687–1709	
RD 9.	Ralf Quast, Ralf Giering, Yves Govaerts, Frank Rüthrich and Rob Roebeling, Climate Data Records from Meteosat First Generation Part II: Retrieval of the In-Flight Visible Spectral Response, Remote Sens. 2019, 11(5), 480; https://doi.org/10.3390/rs11050480	
RD 10.	Govaerts, Yves; Rüthrich, Frank, John, Viju; Quast, Ralf, Climate Data Records from Meteosat First Generation – Part I: Simulation of Accurate Top-Of-Atmosphere Spectral Radiance over Pseudo-Invariant Calibration Sites for the Retrieval of the In-Flight MVIRI/VIS Spectral Response, Remote Sensing **2018**, 10(12), 1959; doi:10.3390/rs10121959.	
RD 11.	SEVIRI Solar Channel Calibration Algorithm Specification Document	EUM/MSG/SPE/411
RD 12.	MTP_CF_to_INGATE_(MPEF)_Interface_Control_Document	EUM/TSS/ICD/14/778737
RD 13.	Image Processing Software Detailed Design Document	MTP/BF/0901/SP/008
RD 14.	MODTRAN V3 solar spectrum, https://agupubs.onlinelibrary.wiley.com/doi/pdf/10.1029/97JD02628, (accessed on 6 December 2018)	
RD 15.	Vermote, E. F., Tanre´, D., Deuze J. L., Herman, M., and Morcrette, J. J. (1997), Second simulation of the satellite signal in the solar spectrum, 6S: an overview.IEEE Trans. Geosci. Remote Sens. 35:675–686.	
RD 16.	Implementing Error Covariances for the Spectral Response function in SSCC, EUM/OPS/DOC/17/896580	
RD 17.	Uncertainty and Error Correlation Quantification for FIDUCEO "easy-FCDR" Products: Mathematical Recipes; http://fiduceo.pbworks.com/w/file/121655436/ErrorCovFormulaeEasyFCDR-v0.8.docx (accessed on 6 December 2018)	

RD 18.	Mathematical notation for FIDUCEO publications; http://fiduceo.pbworks.com/w/file/fetch/121751748/Notation%20FIDUCEO%20v1a.pdf (accessed on 6 December 2018)
RD 19.	Decoster, I.; Govaerts, Y.M.; Baudrez, E.; Dewitte, S.; Velazquez, A.; Blazquez, A.; Cornelis, J. Evidence of pre-launch characterization problem of Meteosat-7 visible spectral response. *Remote Sensing Letters* **2013**, 4, 1008–1017. doi:10.1080/2150704X.2013.828181.
RD 20.	Govarts, Y. M. Correction of the Meteosat-5 and -6 radiometer solar channel spectral response with the Meteosat-7 sensor spectral characteristics. *International Journal on Remote Sensing* **1999**, 10 (18), 3677-3682. doi: 10.1080/014311699211273.
RD 21.	Decoster, I.; Clerbaux, N.; Baudrez, E.; Dewitte, S.; Ipe, A.; Nevens, S.; Blazquez,A.; Cornelis, J. Spectral Aging Model Applied to Meteosat First Generation Visible Band. *Remote Sensing* **2014**, 6, 2534-2571. doi: 10.3390/rs6032534.
RD 22.	BIPM. Evaluation of Measurement Data—Guide to the Expression of the Uncertainty in Measurement. Technical Report JCGM 100:2008 GUM 1995 with minor corrections, 2008.
RD 23.	Hilton, F., et al., 2012: Hyperspectral Earth Observation from IASI: Five Years of Accomplishments. *Bull. Amer. Meteor. Soc.,* **93**, 347–370, doi:10.1175/BAMS-D-11-00027.1
RD 24.	Quast, R.: Spectral Response Uncertainty. Technical Note to EUMETSAT. Archived under the document ID: 1050030.
RD 25.	EUMETSAT Satellites History EUM/OPS/DOC/08/4698
RD 26.	Tahara Yoshihiko and Koji Kato, 2009: New Spectral Compensation Method for Intercalibration Using High Spectral Resolution Sounder, Meteorological Satellite Center Technical Note, No. 52, 1-37.
RD 27.	Press, W.H., S.Teukolksy, W.T. Vetterling and B. Flannery, 1992: Numerical recipes in FORTRAN 77: the art of scientific computing, Second edition, Cambridge University Press.
RD 28.	Hewison, T. J., X. Wu, F. Yu, Y. Tahara, X. Hu, D. Kim and M. Koenig, 2013: GSICS Inter-Calibration of Infrared Channels of Geostationary Imagers using Metop/IASI, IEEE Trans. Geosci. Remote Sens., vol. 51, no. 3, doi:10.1109/TGRS.2013.2238544.
RD 29.	Snel, R.; Lichtenberg, G.; Noël, S.; Krijger, M.; Slijkhuis, K.; Bramstedt, K. Calibration and Monitoring. In SCIAMACHY-Exploring the Changing Earth's Atmosphere; Gottwaldand, M., Bovensmann, H., Eds.; Springer, Dordrecht 2011; doi: 10.1007/978-90-481-9896-2_5.
RD 30.	Space Time Angle Match-up Procedure (STAMP): design and user manual document, EUM/OPS/DOC/13/724358.
RD 31.	Frank Rüthrich, Viju O. John, Rob A. Roebeling, Ralf Quast, Yves Govaerts, Emma Wooliams and Jörg Schulz, Climate Data Records from Meteosat First Generation Part III: Recalibration and Uncertainty Tracing of the Visible Channel on Meteosat-2–7 Using Reconstructed, Spectrally Changing Response Functions, Remote Sens. 2019, 11(10), 1165; https://doi.org/10.3390/rs11101165
RD 32.	Viju O. John, Tasuku Tabata, Frank Rüthrich, Rob Roebeling, Tim Hewison, Reto Stöckli and Jörg Schulz, On the Methods for Recalibrating Geostationary Longwave Channels Using Polar Orbiting Infrared Sounders, Remote Sens., 2019, 11, 1171; https://doi.org/10.3390/rs11101171
RD 33.	Tjemkes, S.A.; König, M.; Lutz, H.-J.; van de Berg, L.; Schmetz, J. Calibration of Meteosat water vapor channelobservations with independent, satellite observations. J. Geophys. Res.2001,106, 5199–520

RD 34.	Tuli, F.T.Z.; Pinto, C.T.; Angal, A.; Xiong, X.; Helder, D. New Approach for Temporal Stability Evaluation of Pseudo-Invariant Calibration Sites (PICS). Remote Sens. 2019, 11, 1502.
RD 35.	Dee D P, Uppala S M, Simmons A J, et al. 2011, The ERA-Interim reanalysis: configuration and performance of the data assimilation system. Quarterly Journal of the Royal Meteorological Society, 137(656): 553–597, doi: https://doi.org/10.1002/qJ.828

APPENDIX A SZA COMPUTATION SOURCE

```
      SUBROUTINE sza(N,M,T,DOY,MSK,LAT,LON,S,Z)
C
C     CALCULATE SZA for N x N pixel
C     Frank Ruethrich EUMETSAT
C     COMPILE WITH:
c     f2py -c -m cruncher cruncher.f
c     DEBUG with:
c     rm *.so
c     f2py -m cruncher -h --overwrite-signature cruncher.pyf cruncher.f
c     f2py -c --debug --build-dir build cruncher.pyf cruncher.f
c     gdb python #then press run timeseries_cruncher.py
c     OR:
c     f2py --debug-capi -c -m cruncher cruncher.f

C
      INTEGER     N,M,DOY
      REAL*8      T(M,M),LAT(N,N),LON(N,N)
      INTEGER     MSK(M,M)

      INTEGER     I,II,J,JJ
      REAL*8      PI
      REAL*8      TORAD
      REAL*8      TODEG
      REAL*8      flNumDayInTheYear
      REAL*8      MSA_EQTIME1
      REAL*8      MSA_EQTIME2
      REAL*8      MSA_EQTIME3
      REAL*8      MSA_EQTIME4
      REAL*8      MSA_EQTIME5
      REAL*8      MSA_EQTIME6
      REAL*8      MSA_DECL1
      REAL*8      MSA_DECL2
      REAL*8      MSA_DECL3
      REAL*8      MSA_DECL4
      REAL*8      MSA_DECL5
      REAL*8      MSA_DECL6
      REAL*8      MSA_DECL7
      REAL*8      flTimeZone

      REAL*8      flRadLat
      REAL*8      flRadLon
      REAL*8      flGamma,flEquTime,flDecli,flTimeOffset
      REAL*8      flTrueSolarTime,flHa,flHaRad,flCosZen
      REAL*8      flTmpZenRad,flTmpZen,flCosAzi,flTmpAzi

      REAL*8      S(N,N)
      REAL*8      Z(N,N)
! Cf2py intent(in) N
! Cf2py intent(in) M

Cf2py intent(in) T
Cf2py intent(in) DOY
Cf2py intent(in) MSK
Cf2py intent(in) LAT
Cf2py intent(in) LON
```

```
Cf2py intent(out) S
Cf2py intent(out) Z
Cf2py integer intent(hide),depend(T) :: M=shape(T,0)
Cf2py integer intent(hide),depend(LAT) :: N=shape(LAT,0)

      PI                =3.14159265359D0
      TORAD             =PI/180.D0
      TODEG             =180.D0/PI
      flNumDayInTheYear=365.D0
      MSA_EQTIME1       =229.18D0
      MSA_EQTIME2       =0.000075
      MSA_EQTIME3       =0.001868
      MSA_EQTIME4       =0.032077
      MSA_EQTIME5       =0.014615
      MSA_EQTIME6       =0.040849
      MSA_DECL1         =0.006918
      MSA_DECL2         =0.399912
      MSA_DECL3         =0.070257
      MSA_DECL4         =0.006758
      MSA_DECL5         =0.000907
      MSA_DECL6         =0.002697
      MSA_DECL7         =0.00148
      flTimeZone        =0.

      DO 5 I=1,N
        DO 6 J=1,N
         IF (N>M) THEN
           II=INT(I/2+1)
           JJ=INT(J/2+1)
         ELSE
           II=I
           JJ=J
         END IF
         IF (MSK(II,JJ).EQ.1) THEN
           flRadLat = LAT(I,J)*TORAD
           flRadLon = LON(I,J)*TORAD
!          Evaluate the fractional year in radians
           flGamma =  2*PI*((DOY)+((T(II,JJ))/24.))/flNumDayInTheYear !checked
!          Evaluate the Equation of time in minutes
           flEquTime = MSA_EQTIME1*(MSA_EQTIME2+MSA_EQTIME3*          !checked
     &dcos(flGamma)-MSA_EQTIME4*dsin(flGamma)-
     &MSA_EQTIME5*dcos(2.*flGamma)-MSA_EQTIME6*
     &dsin(2.*flGamma))
!          Evaluate the solar declination angle in radians */
           flDecli = MSA_DECL1-MSA_DECL2*dcos(flGamma)+MSA_DECL3*     !checked
     &dsin(flGamma)- MSA_DECL4*dcos(2*flGamma)+MSA_DECL5
     &*dsin(2*flGamma)-MSA_DECL6*dcos(3*flGamma)+
     &MSA_DECL7*dsin(3*flGamma)
!          Time offset in minutes equivalent to
!          here was an error
           flTimeOffset = flEquTime-(4.D0*(-1.D0*LON(I,J)))+
     &(60.D0*flTimeZone)!fixed and checked
!          True solar time in minutes */
           flTrueSolarTime = (T(II,JJ)*60.)+flTimeOffset
!          solar hour angle in degrees and in radians
           flHa = (flTrueSolarTime/4.)-180.
           flHaRad = TORAD*flHa
!          Evaluate the Solar local Coordinates
```

```
           flCosZen = (dsin(flRadLat)*dsin(flDecli)+ dcos(flRadLat)*
     &dcos(flDecli)*dcos(flHaRad))
           flTmpZenRad = dacos(flCosZen)
           flTmpZen = TODEG*(flTmpZenRad)
           flCosAzi = -((dsin(flRadLat)*dcos(flTmpZenRad)-
     &dsin(flDecli))/(dcos(flRadLat)*dsin(flTmpZenRad)))
           flTmpAzi =  360. - TODEG*(dacos(flCosAzi))
!        Correct for SZA < 180
           IF (flTrueSolarTime < 720.) THEN
              flTmpAzi = 360. - flTmpAzi
           END IF
           if (LAT(I,J).eq.0.) THEN
!             print*, LON(I,J)," ",flTmpZen," ",flHa," ",flTimeOffset,
!      &" ", flEquTime ," ",flDecli*TODEG
           end if
           S(I,J) = flTmpZen    !checked
           Z(I,J) = flTmpAzi    !checked
!            if (LAT(I,J) > 28.53 .and. LAT(I,J) < 28.57) THEN !for lybia 4
!              if (LON(I,J) > 23.37 .and. LON(I,J) < 23.41) THEN
!                print*, LON(I,J)," ",LAT(I,J)," ",flTmpZen,
!      &" ",flTmpAzi
!              end if
!            end if
         ELSE
           S(I,J) = -999.
           Z(I,J) = -999.
         END IF
6       ENDDO
5     ENDDO
      END
```